DEUTSCHES ELEKTRONEN – SYNCHROTRON

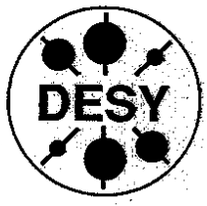

DESY 92–190
December 1992

First Results from HERA

G. Wolf

Deutsches Elektronen-Synchrotron DESY, Hamburg

ISSN 0418-9833

NOTKESTRASSE 85 · D-2000 HAMBURG 52

To be sure that your preprints are promptly included in the
HIGH ENERGY PHYSICS INDEX,
send them to the following (if possible by air mail):

DESY Bibliothek Notkestraße 85 W-2000 Hamburg 52 Germany	DESY-IfH Bibliothek Platanenallee 6 O-1615 Zeuthen Germany

DESY 92-190
December 1992

ISSN 0418-9833

First Results from HERA*

Günter Wolf
Deutsches Elektronen Synchrotron DESY
2 Hamburg 52, Germany

Abstract

The new electron - proton collider HERA at DESY has been put into operation together with the experiments H1 and ZEUS. With HERA, high energy physics has entered a new territory far beyond the reach of previous lepton nucleon scattering experiments. The very first run has already given new results on several topics. Deep inelastic neutral current scattering has been extended by two orders of magnitude towards very small x values. For photoproduction the total cross section has been measured and a large excess of events from hard scattering has been observed. The general characteristics of these hard scatters agrees with the expectations for direct and resolved photon interactions.

1. INTRODUCTION

On May 31st this year, the two HERA experiments H1 and ZEUS observed for the first time electron - proton collisions in their central detectors. This feat was the culmination of eight years of prototyping, construction and commissioning of the machine [1] and the detectors [2,3].

In parallel with the construction of the machine and detectors, the horizon of HERA physics has been substantially expanded as documented in several workshops. The most recent and complete proceedings are those from 1987 (ref. 4) and 1991 (ref. 5).

This report focusses on the results obtained by H1[6] and ZEUS[7] in the first running period in July [8] (partly after this meeting) .

2. THE HERA COLLIDER

2.1 Layout

The layout of HERA is shown in fig.1. Two separate magnet systems guide the e and p beams around the 6.3 km long ring. DESY and PETRA serve as injectors. There are four interaction regions, two of which are occupied by H1 and ZEUS. A third region has been allocated to the experiment HERMES[9] which has been approved recently. Table 1 shows some of the parameters of the collider.

* This report resulted from talks given at the 1992 Aachen Conference on "QCD - 20 years Later", at the 1992 Cargese Institute on "Quantitative Particle Physics" and at the 4th Hellenic School on Elementary Particle Physics, 1992, Corfu.

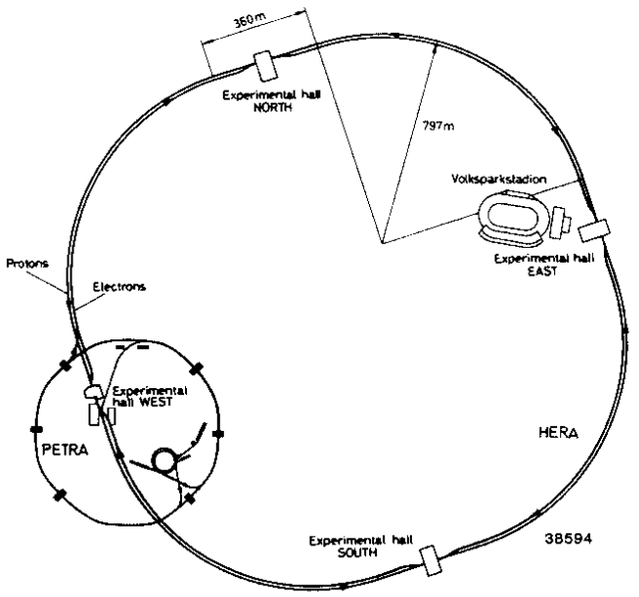

Fig. 1 Layout of HERA

Table 1. HERA design parameters

	electron ring	proton ring
circumference	6336 m	
energy	30 GeV	820 GeV
e - p c.m. energy	314 GeV	
magnetic bending field	0.164 T	4.682 T
bending radius of dipole	610 m	584 m
circulating current	60 mA	160 mA
number of bunch buckets	220	220
number of bunches	210	210
time between beam crossings	96 ns	
luminosity	$1.5 \cdot 10^{31}$ cm^{-2}s^{-1}	
polarization time at E_e = 30 GeV	25 min	

2.2 *Commissioning Phase*

Construction of HERA started in April 1984. In August of 1987 the 6.3 km long tunnel was completed. A year later the electron ring made of normal conducting magnets was put into operation. The proton ring was closed in fall of 1990. Most of the proton magnets are superconducting and are operated at 4.4 K providing a bending field of 4.68 T. The first protons were stored in April 1991 at the injection energy of 40 GeV. Having learned how to accelerate protons and to operate proton and electron beams simultaneously the machine crew began with collision studies. Luminosity was observed for the first time on October 19, 1991 by colliding one electron bunch of 12 GeV with one proton bunch of 480 GeV. The measured luminosity was about $L = 10^{26}$ cm^{-2}s^{-1}. In the following weeks the electron energy, the number of bunches and the beam currents were increased. After reaching $L = 2.10^{28}$ cm^{-1}s^{-1} with 10 bunches per beam at beam energies E_e =

26.6 GeV and E_p = 480 GeV, HERA operations were interrupted and the experiments H1 and ZEUS were installed in the interaction regions during a 4 months shut down.

In April of this year HERA resumed operation. By mid-April electrons were stored at 26.6. GeV; one month later protons were accelerated to the nominal energy of 820 GeV and on May 31st the two experiments registered the first collisions between the two beams. The H1 and ZEUS detectors were brought on-line concurrently with the beam tests of HERA: no special running period was provided for running-in or tuning of the detectors. Data taking started at the end of June with 10 bunch operation, maximum beam currents of 1 - 2 mA and maximum luminosities around $6.10^{-28}cm^{-2}s^{-1}$. In a first one month long period data were recorded for integrated luminosities of 2 - 3 nb^{-1}. Physics results from this running period were reported a week after data taking has finished[6,7].

After a shut down and machine tests a second data taking period from mid-September until beginning of November followed.

2.3 Performance

The construction of HERA presented the machine builders with many challenges. Some of these will be briefly discussed.

Superconducting magnets. HERA has been the first accelerator where the superconducting magnets have been built in industry. The design of the dipole magnets has started with that from the FNAL magnet, changing in the course of the development from a warm to a cold iron yoke. Production procedures for dipoles were developed at DESY. Following the construction of prototype magnets at DESY and in industry, the 422 dipole magnets were built by Ansaldo (Italy) and ABB (Germany). The quadrupoles were developed and prototypes were constructed by Saclay. The 224 quadrupoles were built by KWU + Noell (Germany) and Alsthom (France). The dipoles and quadrupoles delivered exceed the required operating currents and fields by more than 30%.

Persistent sextupole currents. Protons are injected into HERA from PETRA at an energy of 40 GeV which is a factor of 20 lower than the operating energy of 820 GeV. At 40 GeV persistent currents producing a sextupole component in the dipole magnets present a major disturbance. However, the persistent current sextupole varies little from magnet to magnet and is well reproducible. It is compensated by correction coils wound directly on the dipole and quadrupole beam pipes. Flux creep in the superconductor and other effects cause the magnetization currents to decay approximately logarithmically in time. This drift is also compensated using the correction coils. The required strength of the correction elements at injection and during acceleration is determined by measuring continuously the dipole and sextupole fields in two reference magnets, powered in series with the ring magnets.

Superconducting cavities. The power lost by the electron beam due to synchrotron radiation amounts to 7.6 MW at 30 GeV and 60 mA beam current. Up to ~ 28 GeV the energy loss is compensated by 88 normal conducting cavities recuperated from PETRA. For higher energies eight 2 x 4 cell superconducting cavities operating at

500 MHz were developed and built in industry. Without beam they provide an accelerating gradient of 5 MV/m.

Proton beam stability. The lifetime of the proton beam in single beam operation is well above 100 h. In colliding beam mode lifetimes in excess of 50 h have been obtained regularly. While the transverse size of the electron beam is limited by synchrotron radiation, no such mechanism is operative for protons. The longitudinal bunch length can be limited to ~ 10 cm (rms) by operating the 52 MHz and 208 MHz RF systems concurrently. For the first two data taking periods this was not done routinely. Typical bunch lengths were 12 - 50 cm. Since the bunch length of the electron beam is much smaller (~ 8 mm rms) the interaction volume was half of the proton bunch length, i.e. 6 - 25 cm (rms).

In operations with 10 consecutive bunches no bunch - bunch interactions were observed for either the electron or the proton beam. With increasing number of bunches bunch - bunch interactions are expected to occur. Feed back systems which had been tested in PETRA were installed in HERA to counteract these collective effects.

Luminosity. The design value for the specific luminosity (luminosity per bunch and mA bunch currents) is 4.4 10^{29} $cm^{-2}s^{-1}$ mA^{-2}. This value was achieved in the operation with 10 on 10 bunches and beam currents of up to 3 mA. The maximum luminosity observed to date was 4.10^{29} $cm^{-2}s^{-1}$. The average luminosity collected by the experiments per day has increased by roughly a factor of 7 from the first to the second run period (see fig. 2).

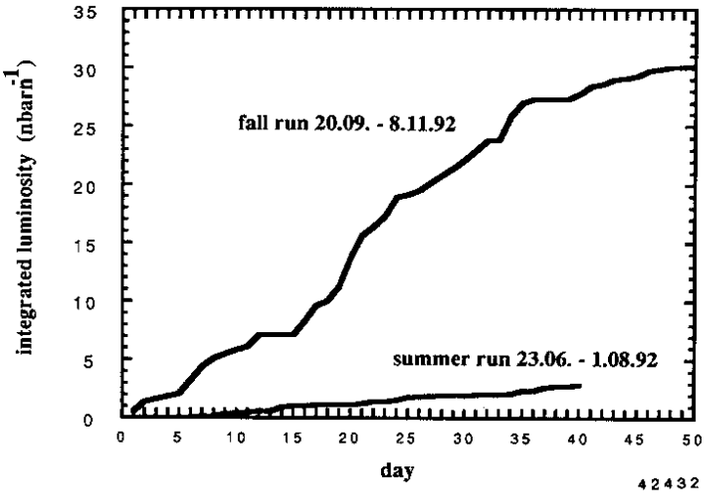

Fig. 2 Luminosity per day collected by ZEUS during the first and second running period (from U. Schneekloth).

A major limitation of the luminosity was a limit on the electron current of about ~ 7 mA beyond which the electron beam lifetime rapidly approached zero. During the last machine shifts before the winter shut down the cause was finally traced back to a faulty pump. After replacement electron currents of up to 23 mA in 110 bunches could be stored. On the proton side up to 160 bunches were filled with a total current of 13 mA. Thus an increase of the luminosity by an order of magnitude can be expected for the next running period.

Polarization. After coasting for some time the electrons become polarized with spins being antiparallel to the direction of the bending field as a result of the Sokholov - Ternov effect [10]. The build - up time for the polarization is determined by the synchrotron radiation and is given by $P(t) = P_0 (1- \exp (-t/t_p))$ with $P_0 = 92\%$ and $t_p = 98\ r^2\ R\ E^{-5}$, t_p in s, r bending radius in m, R average radius in m and E electron beam energy in GeV. This prediction holds for a perfect machine. Already small imperfections e.g. in the magnet lattice may produce depolarization effects and make the depolarization time shorter than the build-up time thereby destroying the polarization. Only a few shifts were devoted sofar to the study of beam polarization. An electron energy near 26.67 GeV was chosen. Beam polarization in HERA was observed for the first time in fall of 1991 at the level of P = 5 - 9%. After realignment of magnets P increased to 18% by April 1992. After the summer shutdown and with some tuning suggested by tracking programs a polarization of 58±5% was measured[11] (see fig. 3).

For particle physics, instead of transverse polarization electrons of definite helicity (left - or right handed) are needed. This can be achieved with the help of a pair of spin rotators installed at the interaction regions. A pair of spin rotators was designed and built[12] and is available for installation and testing in HERA.

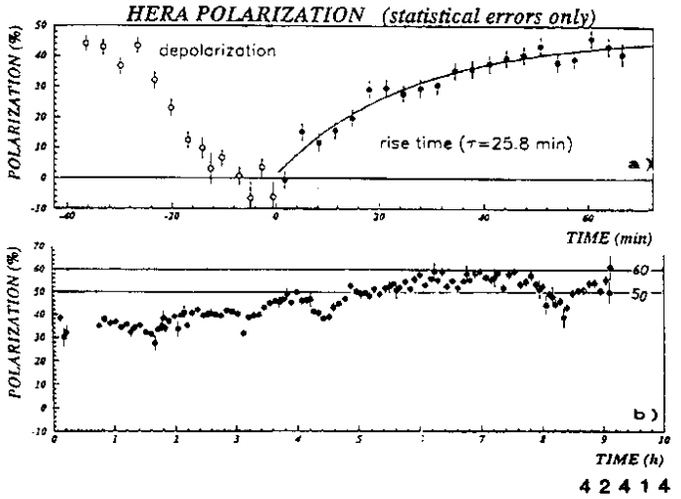

Fig. 3 a) The transverse electron polarization at E_e = 26.7 GeVas a function of time.
b) Beam polarization during a long fill.

3. THE EXPERIMENTS

3.1 Detector Challenges

HERA produces a large variety of reactions with widely differing energy flows. This feature together with the desire for detecting and identifying the constituents such as electron, photon, quarks and gluons which participate in these reactions places different requirements on the detector. The large momentum imbalance between incident electrons and protons and the nature of space - like processes send most particles into a narrow cone around the proton

direction. The observation of deep inelastic (DIS) neutral current (NC) scattering, e p -> e X (fig. 4a), is fairly straightforward. It produces a high energy electron whose transverse momentum is balanced by the current jet. The remants from the breakup of the proton escape mostly unseen down the beam pipe. The variables x and Q^2 which describe the process (see below) can be determined from the energy and angle of either the electron or the current jet. This requires a precise electromagnetic and hadronic calorimeter with the calibration known at the 1 - 2% level.

In charged current (CC) scattering, e p -> ν X (fig. 4b), only the current jet can be observed. The idendification of such events is based on the observation of missing transverse momentum carried away by the neutrino. It requires a hermetic calorimeter which covers the full solid angle such that e.g. photons, neutrons or K^o_2 cannot escape undetected. The variables x and Q^2 are measured from the current jet.

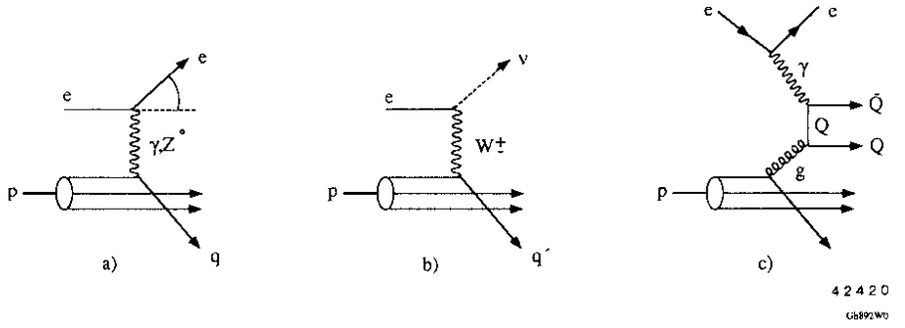

Fig. 4 Diagrams for NC and CC scattering and for photon - gluon fusion

The observation of processes at low Q^2, in particular from scattering on soft partons or from production of pairs of charm or bottom mesons (fig. 4c) is more difficult. The energy deposited in the calorimeter often is only a few GeV. Additional information from tracking detectors which surround the interaction point is necessary for their identification.

Background presents another challenge. The number of events from e - p interactions is tiny (10^{-3} - 10^{-5}) compared to the background events produced for instance by beam protons on the beam pipe wall or in the residual gas. What is worse, this type of background deposits a large amount of energy in the detector. A typical background event is shown in fig. 5 where 225 GeV are observed in the calorimeter and many tracks in the tracking detector. At proton design current the background rate is expected to be around 10 - 100 kHz. The detector must be able to discriminate quickly - within a few microseconds - against background events although both beams cross each other every 96 ns. The high background rates combined with the short bunch crossing interval forced the HERA experiments to develop novel concepts of electronic readout and triggering, concepts which are suitable also for detectors at the next generation of pp colliders, SSC and LHC.

The H1 and ZEUS detectors are driven by their choice of calorimeter. ZEUS uses a compensating uranium - scintillator calorimeter which provides the best possible energy resolution for hadrons. Compensation means that electromagnetic particles (electrons, photons) and hadrons of the same energy yield the same pulse height, e/h = 1. The radioactivity of the (depleted) uranium provides an extremely stable calibration signal, the mean life time of ^{238}U being $6.5 \cdot 10^9$ years. The H1 calorimeter uses liquid argon for readout which promises a very stable and precise energy calibration and allows a high transverse and longitudinal segmentation. The calorimeter is noncompensating, e/h = 1.1 - 1.2. However, due to the high segmentation and using software weighting with the observed shower profile equal signals for electrons and hadrons can be obatined.

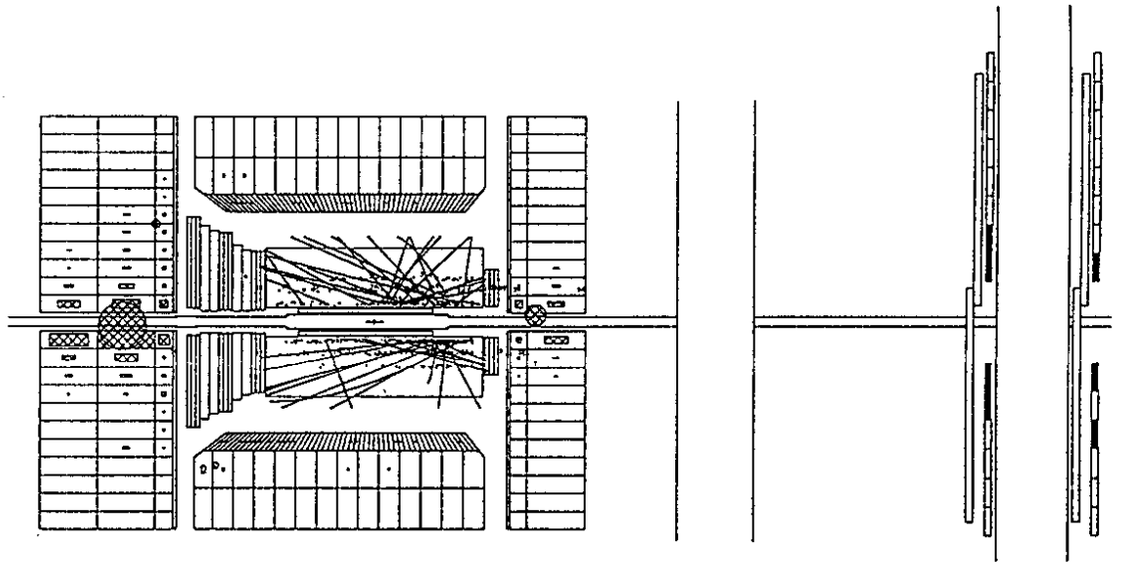

Fig. 5 A background event produced by a proton interaction upstream (to the right) of the ZEUS detector

3.2 The H1 Detector

The H1 detector[2] is displayed in fig. 6. The liquid - argon calorimeter (LA) covers the angular region $4^0 < \Theta < 155^0$ (the foward direction, $\Theta = 0^0$, is given by the direction of the proton beam). The calorimeter is longitudinally subdivided into an electromagnetic section with lead plates and a hadronic section with stainless steel plates as absorbers. The total depth varies between 8 and 4.5 absorption lengths. The calorimeter was optimized for a precise measurement and identification of electrons and for a stable energy calibration for electrons and hadrons. The energy resolution σ/E for electrons is $12\%/\sqrt{E} \oplus 1\%$ ($\oplus$ means quadratic addition) and $45\%/\sqrt{E} \oplus 1\%$ for hadrons (after weighting) as measured with test beams (fig. 7). The calorimeter has been in operation since April 1991. Since then the charge collection has changed by less than 0.2% and the number of

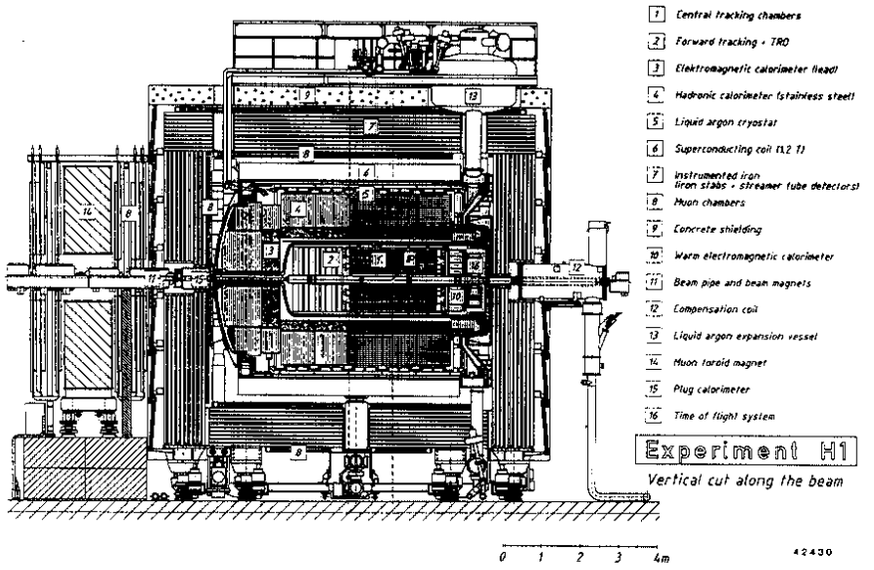

Fig. 6 Schematic view of the H1 detector.

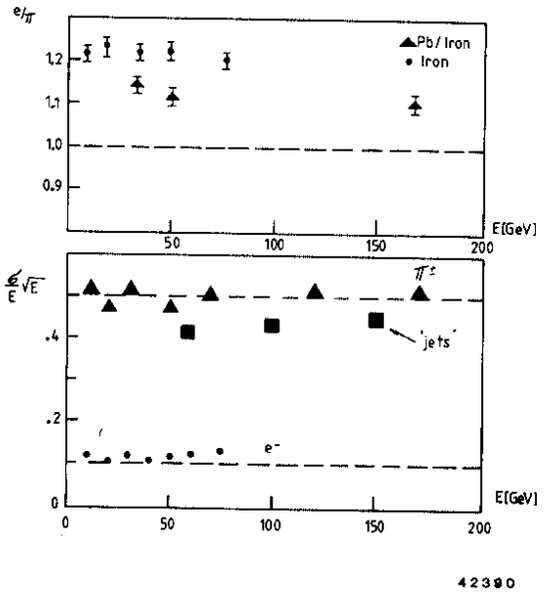

Fig. 7 Test beam results for the H1 calorimeter. Top: e/π ratio, bottom: energy resolution for electrons and hadrons (after software weighting).

dead or problematic readout channels is below 0.1%.

In the backward direction the calorimeter is supplemented by an electromagnetic lead - scintillator calorimeter (BEMC) followed by time-of-flight counters (TOF-VETO). In the forward direction the plug calorimeter with copper plates and silicon diode readout extends the energy measurement for hadrons down to angles of 0.7^{o}.

Charged particles are tracked in a magnetic field of 1.2 T which is produced by a superconducting solenoid that surrounds the calorimeter. The tracking system consists of cylindrical jet - and z - drift chambers in the central region, and of three radial and three planar drift chambers in the forward direction. The drift chambers are interleaved with proportional wire chambers for a fast trigger selection. The backward direction is covered by a four layer proportional wire chamber providing space points up to a scattering angle of 175^{o}. In forward direction a transition radiation detector (TRD) enhances the electron identification.

The magnet yoke is made of 10 layers of 7.5 cm thick iron plates. The gaps are instrumented with limited streamer tube (LST) chambers for measuring energy which has not been fully absorbed in the liquid argon calorimeter and for tracking of muons. Large area LST chambers in front and behind the iron yoke and an iron toroid magnet plus 6 layers of drift chambers in forward direction complete the muon detection system.

The luminosity is measured by observing the bremsstrahlung process e p -> epγ at very small angles to the electron beam direction. The final state electron and photon are detected in coincidence in electromagnetic calorimeters of the luminosity detector LUMI positioned at 33 m (electron tagger) and 100 m (photon tagger) upstream (in proton direction) of the central detector (fig. 8). At nominal luminosity the rate of luminosity events is between 50 - 100 kHz depending on the selection criteria.

Figure 9 shows the H1 detector on its way into the interaction region.

The H1 collaboration at present consists of 320 physicists from 32 institutes and 11 countries.

3.3 *The ZEUS detector*

A cross section of the ZEUS detector[3] along the beams is shown in fig. 10. The main component is the uranium - scintillator calorimeter (CAL) subdivided mechanically into the forward (FCAL), barrel (BCAL) and rear (RCAL) calorimeters. The CAL covers polar angles from 2.6^{o} to 176.1^{o} and 99.7% of the total solid angle. It consists of a total of 80 modules. Every module is made of up to 180 layers of 3.3 mm thick depleted uranium plates plus 2.6 mm thick scintillator plates. Wave - length shifter bars transport the light to photomultipliers. The modules are subdivided longitudinally into an electromagnetic and two (one) hadronic sections in FCAL, BCAL (RCAL) presenting a total depth of 7 to 4 absorption lengths. The scintillator plates form 5 x 20 cm^2 (10 x 20 cm^2) cells in

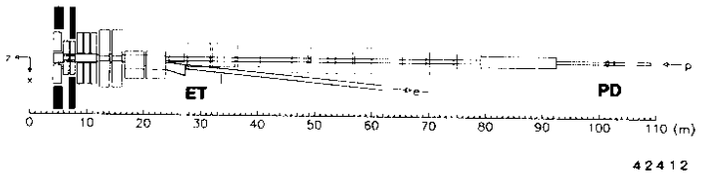

Fig. 8 Layout of the H1 luminosity detector.

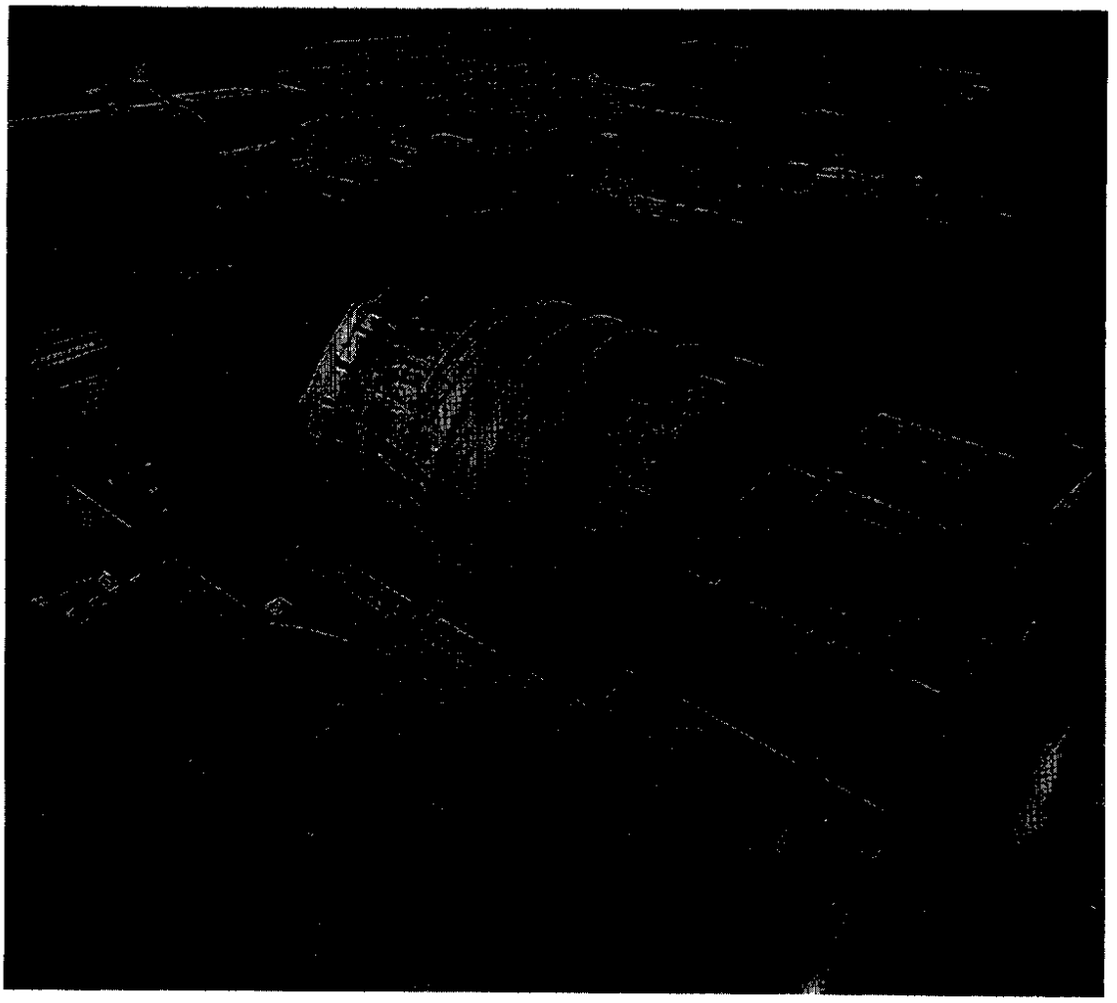

Fig. 9 The H1 detector on its way to the beam position.

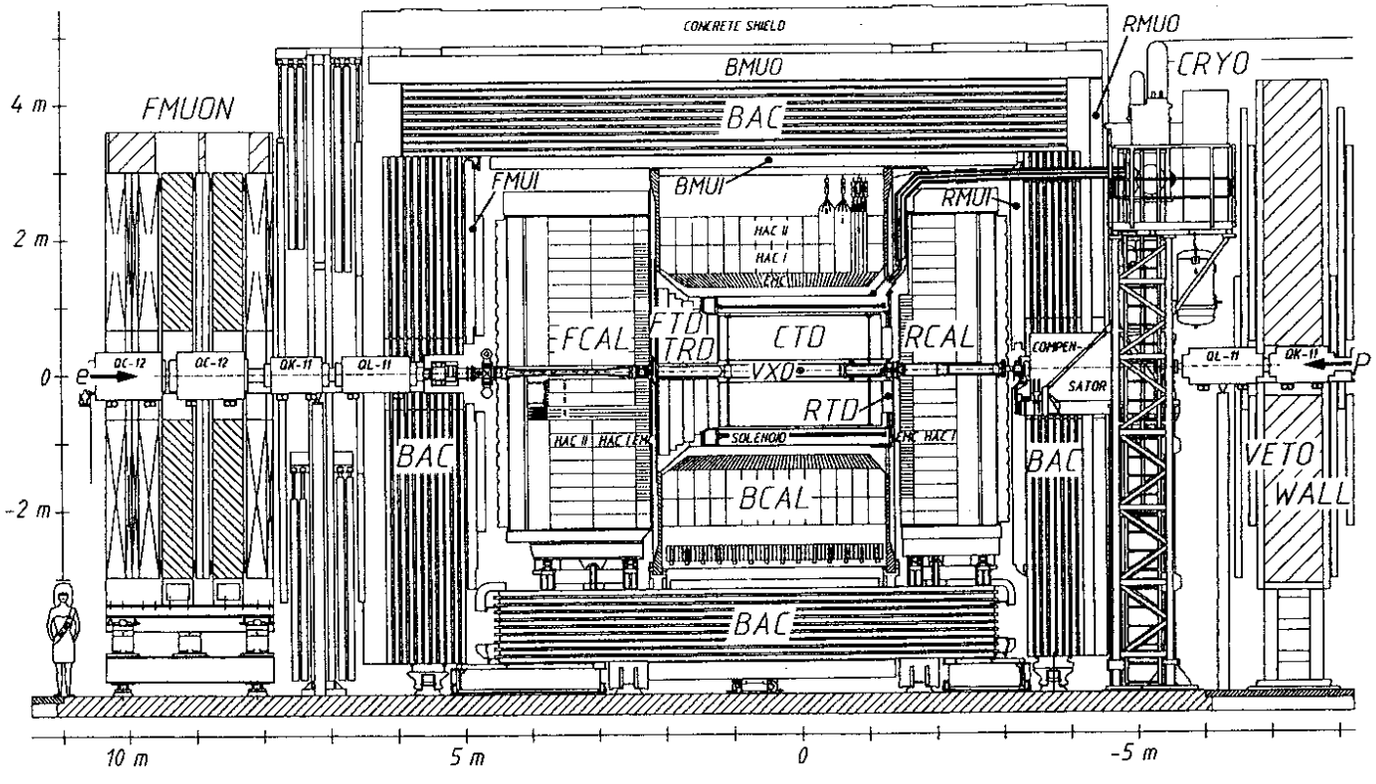

Fig. 10 Cross section of the ZEUS detector

the electromagnetic section and 20 x 20 cm^2 in the hadronic sections of FCAL, BCAL (RCAL).

The calibration of the photomultipliers is being monitored with the signal (UNO) from the radioactivity of the uranium to a precision of < 0.2%. The pulse heights of electrons and hadrons (fig. 11a) are equal to within 3%, i.e. e/h = 1.0 ± 0.03 (fig. 11b), for momenta above 3 GeV/c. The energy resolution as measured in the test beam is for electrons $\sigma/E = 18\%/\sqrt{E}$ (E in GeV) and for hadrons $35\%/\sqrt{E}$ (fig. 11c). The calorimeter yields also an accurate time measurement. The time resolution of a calorimeter cell is $1.5/\sqrt{E} \oplus 0.5$ ns or < 1 ns above 3 GeV.

In the course of an upgrade program, the transverse segmentation of the forward and rear parts of the calorimeter is being increased by inserting a plane of 3 x 3 cm^2 silicon diodes after the first 3 radiation lengths.

Charged particles coming from the interaction point are detected in the tracking system. It consists of a vertex detector, a cylindrical jet - type drift chamber and planar drift chambers in the forward and backward directions. In the forward direction planar transition radiation chambers are used for enhanced electron identification. The tracking detectors are surrounded by a thin - walled solenoid which produces a magnetic field of up to 1.8 T.

The iron yoke serves as the absorber for the backing calorimeter and as a muon filter. It is made of 7.5 cm thick iron plates and instrumented with proportional tube chambers for measuring the energy not absorbed in the uranium calorimeter. For identification and momentum measurement of muons the yoke is magnetized to 1.6 T with copper coils. Large area LST chambers measure the position and direction of muons in front and behind the iron yoke. In the forward direction a spectrometer of two iron toroids and drift - and LST chambers identifies muons and measures their momenta up to 100 - 150 GeV/c.

For luminosity measurement the same reaction and a setup similar to that of H1 is used.

Very forward scattered protons (transverse momenta < 1 GeV/c) are measured in the leading proton spectrometer which uses the proton ring magnets for momentum analysis and detects the scattered protons in 6 stations with silicon strip detectors mounted very close to the beam at distances between 26 and 96 m. The stations have been installed, the detectors not yet.

Particles produced by the proton beam upstream of the detector are detected in the VETOWALL. For monitoring the time structure and other properties of the two beams a ring counter C5 has proven to be invaluable. It is made of two lead - scintillator layers and mounted on the beam pipe behind RCAL. C5 registers the halo particles accompanying both beams.

The central detector of ZEUS is shown in fig. 12.

The ZEUS experiment is performed by a joint effort of 450 physicists from 11 countries and more than 50 institutes.

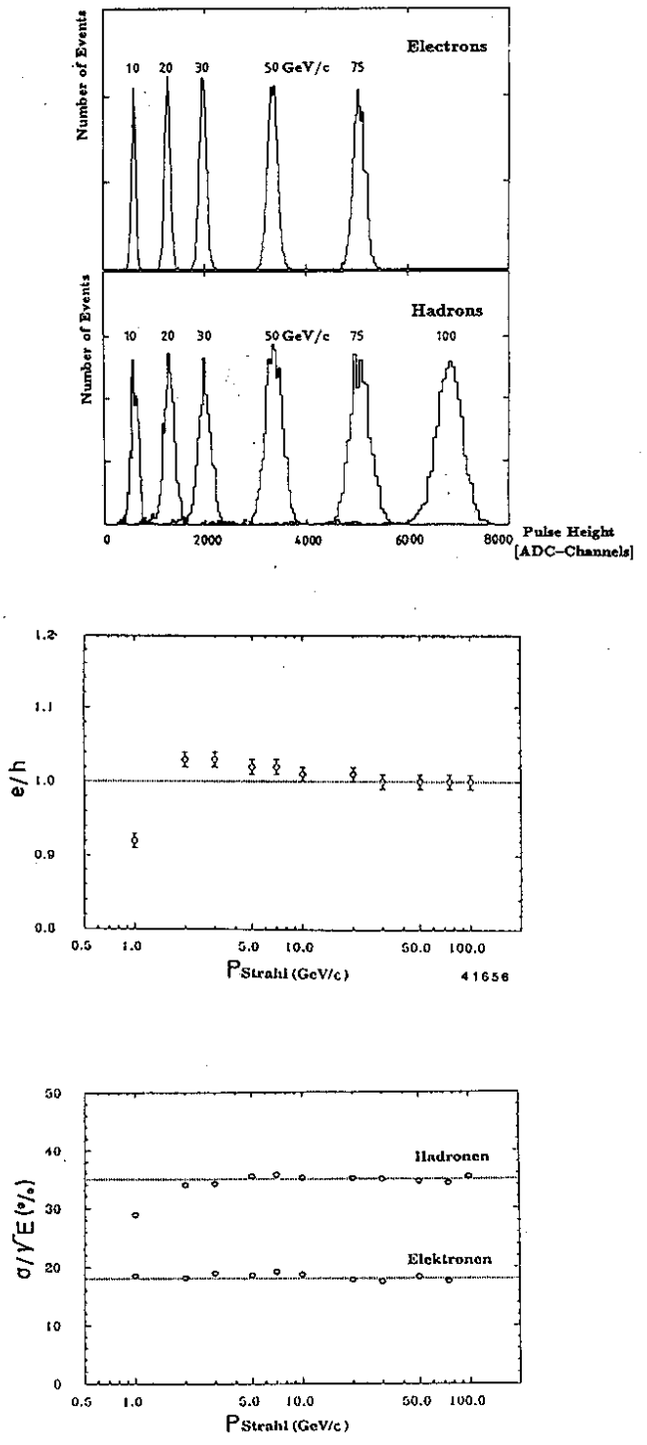

Fig. 11 Measurements with the ZEUS prototype calorimeter:
(a) Pulse height distributiuons for electrons and hadrons;
(b) Energy resolution for electrons and hadrons, and, (c) e/h ratio as a function of momentum

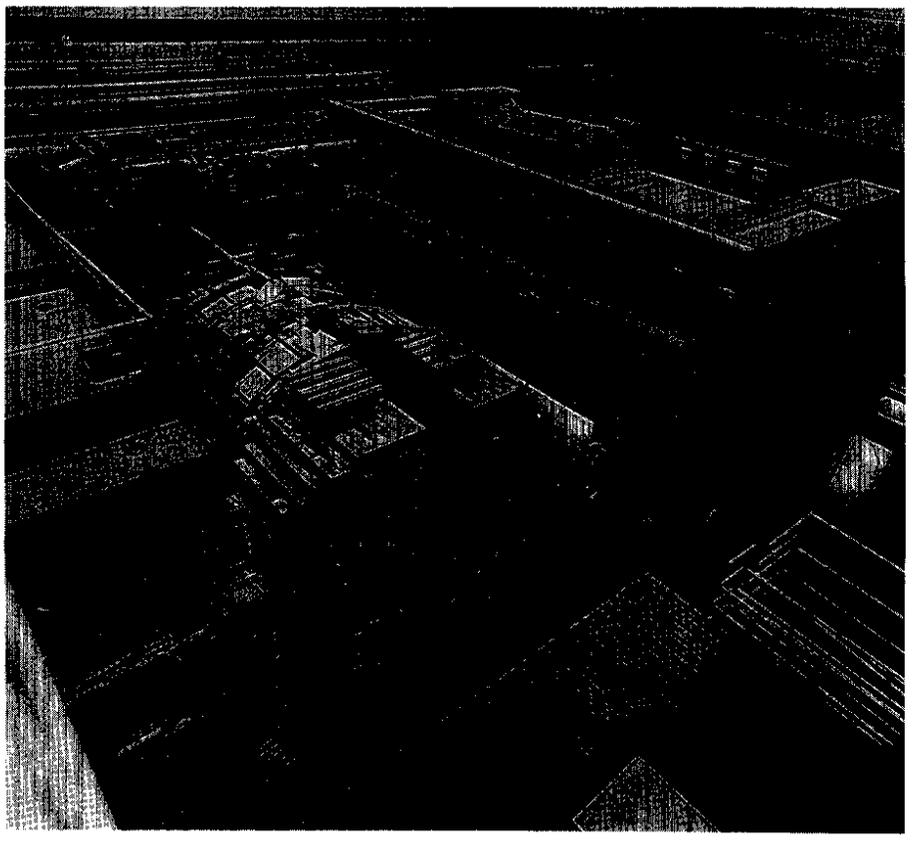

Fig. 12 View of the ZEUS detector: in the foreground the uranium - scintillator calorimeter

3.4 Trigger Selection

The selection of interesting events during data acquisition proceeds in four (three) trigger steps for H1 (ZEUS). The selection at trigger level one is made after 2.4μs (H1) and 4.4 μs (ZEUS), respectively. Up to this point information from 200 000 to 300 000 electronic channels are stored dead time free in analog or digital pipelines for 25 (H1) and 46 (ZEUS) consecutive beam crossings, respectively. Global information from various components like the calorimeter energy sums obtained by summing over specific regions of the calorimeter are stored in trigger pipelines. In case an interesting event is detected, the signal pipelines are stopped and the data for the bunch crossing(s) in question are digitized. The digitized data are used on the next trigger level(s) for a more restrictive event selection.

The final event selection is done in computer farms. At this point the complete digitized information for the event is available and a first reconstruction of the event is performed. The filter farms consist of a large number of fast processors with computing power of ~ 300 (H1) to 1000 MIPS (ZEUS), each processor processing one event at a time. The rate of accepted events varies in both experiments between about 3 and 7 Hz; typical event sizes are 60 kByte (H1) to 140 kByte (ZEUS). The accepted events are reconstructed off-line in processor farms with sufficient computing power to have the reconstructed events available for analysis within a few hours after data taking.

4. RUNNING CONDITIONS

The typical bunch configuration of HERA during the first weeks of data taking is sketched in fig.13: 10 consecutive proton bunches (1 - 10) and 9 electron bunches (1 - 9) are filled. The 10th proton bunch is unpaired; it has no electron partner and is used for studying proton beam induced background. Similarly, the electron bunch 19 is unpaired and is used to measure electron beam induced background. Typical beam currents were 1 - 2 mA.

The luminosity was measured by detecting the process ep -> e'p γ as mentioned before. Figure 14 shows the scatter plot of the energies E_e', E_γ for the final state electron and photon as determined by the luminosity detector. There is a well isolated band of events for which the sum of the two energies is equal to the energy of the electron beam, $E_e' + E_\gamma = E_e$, as expected for the luminosity reaction. However, bremsstrahlung of the electron beam on the residual gas in the beam pipe, e A -> e' A' γ, satisfies the same condition. The subtraction of this background was done by measuring the gas bremsstrahlung with the unpaired electron bunch and scaling with the currents of the unpaired electron bunch and the total electron beam (see fig. 15). The achieved precision of the luminosity measurement is at present 10 - 15%.

The total integrated luminosity collected in the first running period was about 3 nb^{-1} for each of the two experiments, 50 - 75% of which was used for physics analysis.

Suppression of background events at the trigger stage to a manageable rate was not a particularly difficult task, mostly because the beam currents were only a few percent of their nominal values. By far the most copious background was produced by proton interactions upstream of the detector (see fig. 5). The strategies for suppressing unwanted background and selecting electron - proton collisions were different for the two experiments.

4.1 ZEUS Data Taking

In the ZEUS experiment, the trigger selection was made on the basis of

- energies and arrival times measured in the calorimeter,
- energy detected in the electron calorimeter of LUMI,
- veto signals from the C5 counter or the VETOWALL.

The calorimeter time information has turned out to be a powerful handle for rejecting proton beam background. This is illustrated in fig. 16. In an ep collision particles are emitted from the interaction point, IP, and arrive at the calorimeter cells at times t = 0 while a proton interaction upstream of the detector such as shown in fig. 5 deposits energy in the RCAL about 10 ns *earlier*. The 10 ns difference corresponds to twice the distance between RCAL and the IP. Of course, in FCAL also the proton induced background arrives at t = 0. The measured distribution of FCAL (t_{FCAL}) versus RCAL (t_{RCAL}) times is shown in fig. 16 for events with more than 1 GeV deposited in a calorimeter cell in both FCAL and

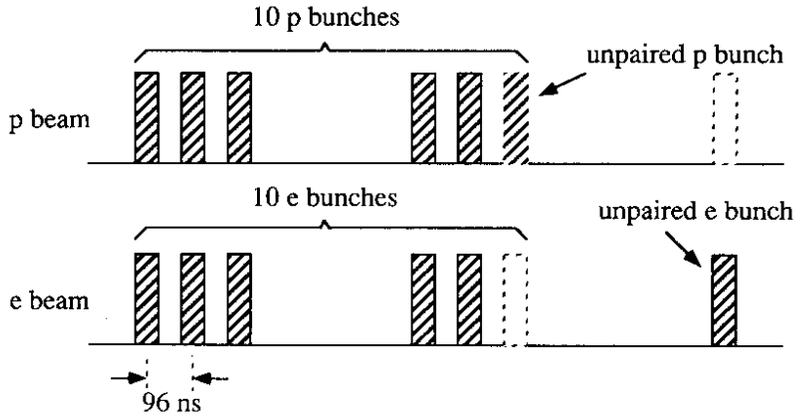

Fig. 13 Sketch of the HERA bunch configuration

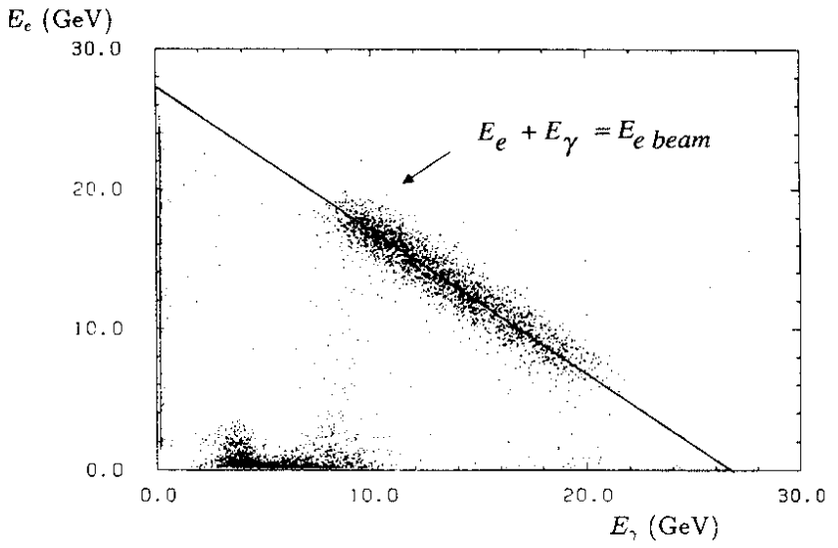

Fig. 14 Distribution of the electron energy versus the photon energy measured in the ZEUS luminosity detector

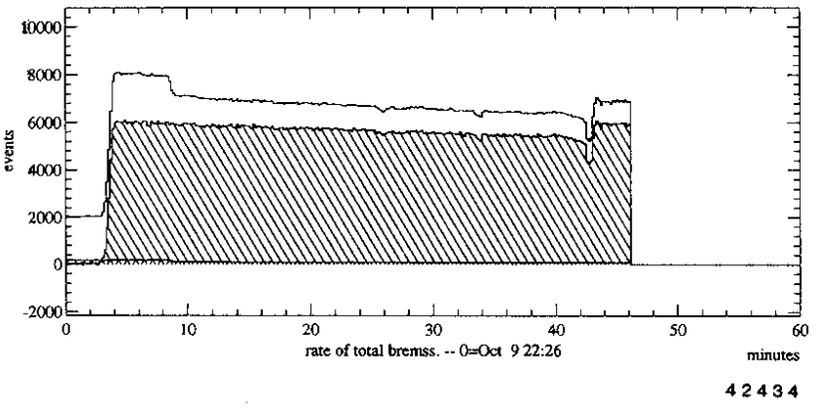

Fig. 15 The total bremsstrahlung rate (upper curve) and the luminosity after subtraction of beam gas bremsstrahlung (lower curve) as a function of time (from ZEUS)

RCAL. The ep events with $t_{FCAL} \sim t_{RCAL} \sim 0$ are well separated from the background which clusters around $t_{RCAL} = -10$ ns, $t_{FCAL} - t_{RCAL} = 10$ ns. Note, there are about 1000 times more background than ep events.

Samples of event pictures are shown in fig. 17. The first event stems from neutral current scattering at $Q^2 \approx 2550$ GeV^2, $x \approx 0.07$, with an electron seen in BCAL and a high energy jet in FCAL (fig. 17a). The jet near the proton beam is presumably produced by the proton remnants. The high energy jet and the electron are back-to-back in the transverse plane and balance transverse momentum as expected for an NC event. The interaction point is marked by tracks detected in the cylindrical drift chamber (CTD). The second event (fig. 17b) shows a low Q^2, low x event ($Q^2 = 6$ GeV^2, $x = 0.0004$). The electron is produced very close to the beam and is only seen in RCAL. The third event (fig. 17c) is due to quasireal photoproduction: it has energy deposition and charged tracks in the central detector plus an electron of 10.5 GeV in the LUMI electron calorimeter. The c.m. energy of the photon - proton system for this event is 230 GeV; the equivalent proton energy for a stationary proton would be 28 TeV.

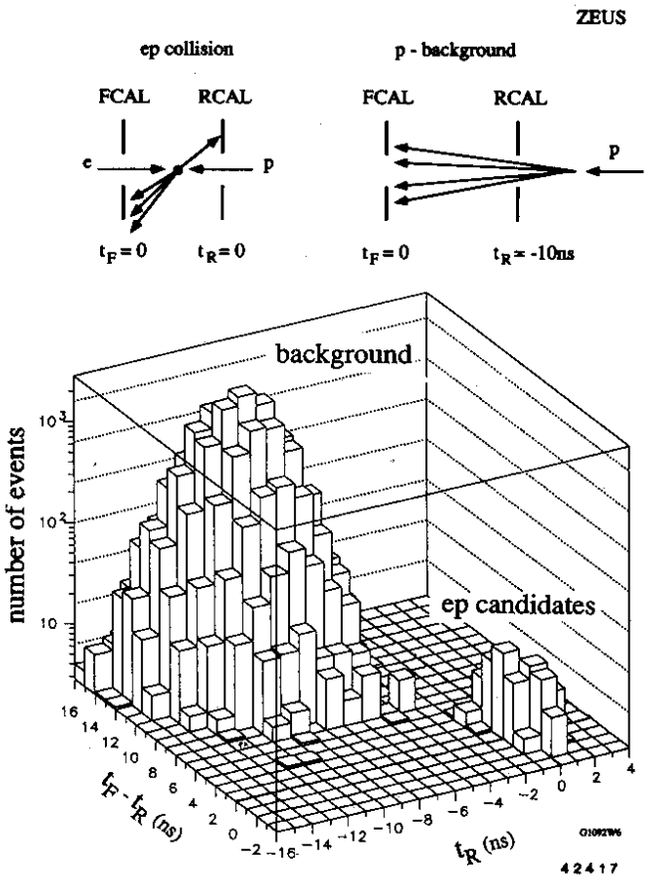

Fig. 16 Distribution of the signal time measured by ZEUS in the RCAL (t_R) versus the difference $t_F - t_R$ between signal times seen in FCAL and RCAL

The event pictures were produced by including every calorimeter cell with an energy more than 60 (100) MeV in the electromagnetic (hadronic) section. The

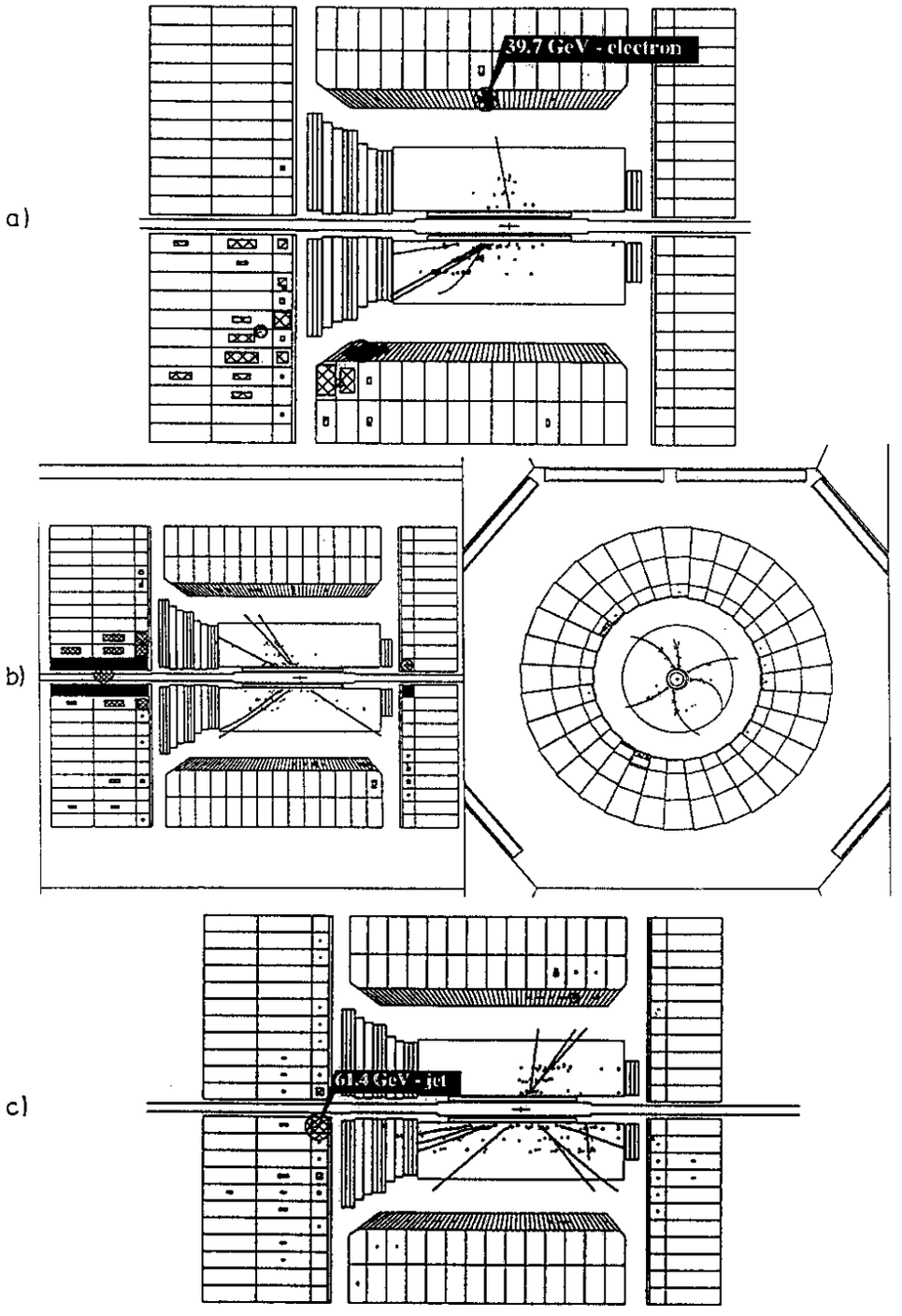

Fig. 17 Event pictures observed by ZEUS:
a) Deep inelastic NC scattering at $Q^2 \approx 2550$ GeV^2, $x \approx 0.07$
b) Deep inelastic NC scattering at $Q^2 \approx 6$ GeV^2, $x \approx 0.0004$
c) Photoproduction at a total c.m. energy of 230 GeV

calorimeter is seen to be very clean. The information on charged particle tracking is still limited due to missing digitizing electronics which is scheduled for installation later this year and during 1993. For the moment the CTD provides only z and r-phi coordinates from the z-by-timing readout of 16 wire layers in superlayers 1, 3 and 5. Since the start of the second running period tracks are also recorded by the vertex detector.

The rate of background events hitting the detector was around a kHz. It was reduced by the first level trigger to 10 - 15 Hz and to 3 - 5 Hz at the third level. In total about 10^6 events were recorded. About 1000 events were selected as ep collisions for an integrated luminosity of 2.5 nb^{-1}.

4.2 H1 Data Taking

The suppression of background at the trigger stage was accomplished in the H1 experiment with the help of

- the scintillator hodoscope in the backward direction (TOF - Veto),
- the proportional wire chambers of the central tracker requiring at least one ray pointing to the vertex region,
- the liquid-argon (LA) and backward electromagnetic calorimeters
- (BEMC) requiring clusters of > 8 (4) GeV in the first (second) component.
- the electron calorimeter of LUMI.

The readout of the tracking system is rather complete and well understood. A spectacular event produced by a proton interaction on the rest gas in the beam pipe is shown in fig. 18. It has 21 protons identified via dE/dx in the central jet chamber. The dE/dx distribution for background events shows well isolated bands of π, K, p and d (fig. 19).

The overall response of the detector is illustrated in fig. 20 with events from NC scattering and photoproduction. The high longitudinal and transverse segmentation of the liquid argon calorimeter gives a detailed account of the energy deposition for single particles and jets.

The rate of background events in the detector was ~ 3 kHz; this was reduced to 20 Hz and 3 - 5 Hz at the first and fourth trigger levels, respectively. A total of 5.10^6 events were recorded. The event sample used for the physics analysis corresponds to an integrated luminosity of 1.5 nb^{-1}.

5. DEEP INELASTIC ELCTRON PROTON SCATTERING

5.1 Physics Introduction

The incoming electron couples to the electroweak current j which probes the structure of the proton. The neutral (NC) and charged (CC) components of the current can be distinguished by the observation of the final state electron or neutrino. The basic deep inelastic scattering process (DIS) is illustrated in fig. 21.

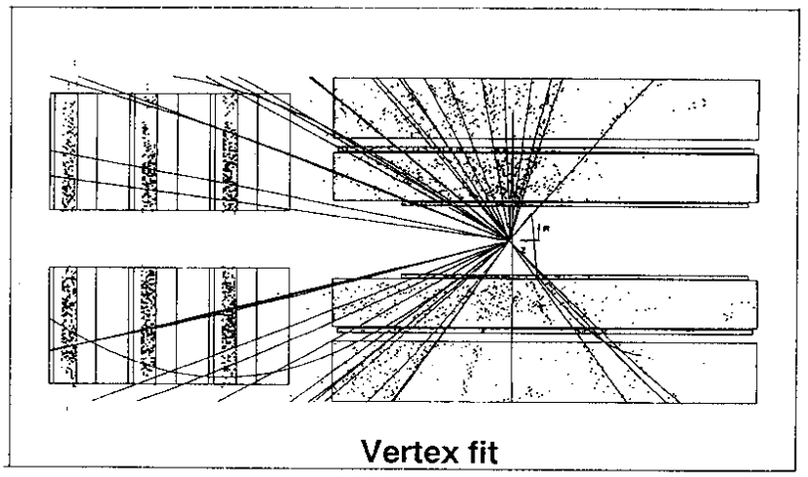

Fig. 18 Example of a proton - gas interaction in the H1 detector with 21 final state protons identified by dE/dx

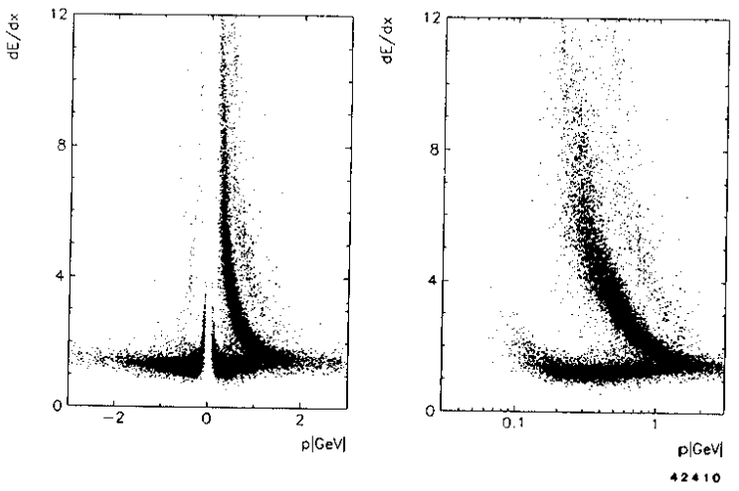

Fig. 19 dE/dx spectra observed by the central tracker of H1 for negative and positive particles

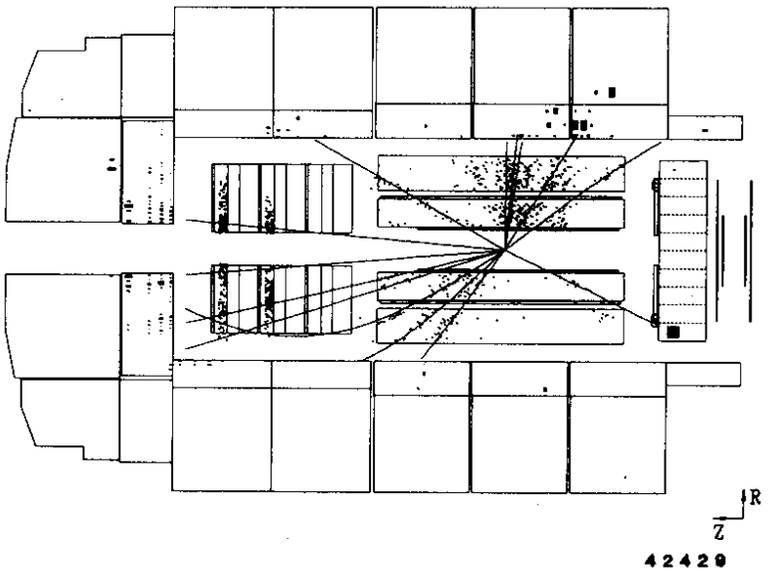

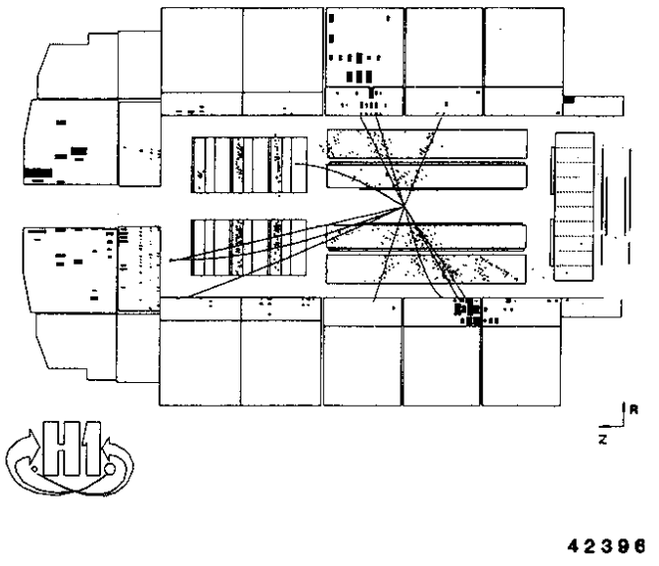

Fig. 20 Event pictures observed by H1:
a) Deep inelastic NC scattering at $Q^2 = 103\ GeV^2$, $x = 0.004$
b) Photoproduction with two jets in the final state

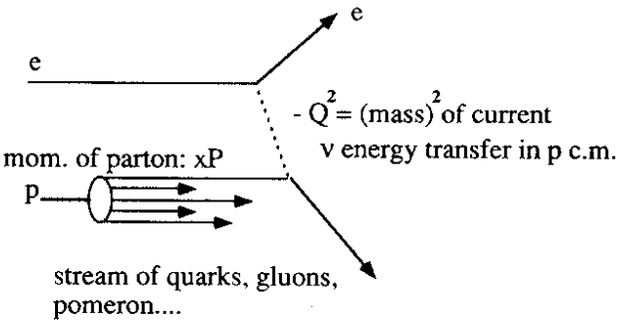

Fig. 21 Diagram for ep scattering

5.1.1 Kinematics

The relevant kinematic variables are

E_e, E_p	electron and proton beam energies
$s = (e + p)^2 = 4 E_e E_p$	square of the total c.m. energy
$q^2 = (e - e')^2$	
$= - 2 E_e E_{e'} (1 + \cos \theta_{e'}) = - Q^2$	square of four momentum transfer
$Q^2_{max} = s$	maximum possible Q^2 value
$\nu = q \cdot p / m_p$	energy of current j as measured in rest system of the incoming proton
$\nu_{max} = s/(2m_p)$	maximum energy transfer
$y = (q \cdot p) / (q \cdot e) = \nu/\nu_{max}$	fraction of energy transfer
$x = Q^2 / (2 q \cdot p) = Q^2 / (2 m_p \nu)$	Bjorken scaling variable and fraction of
$= Q^2 / (y s)$	the proton momentum carried by the struck parton
$\Delta = \hbar/Q$	smallest size of objects that can be resolved in the proton

where $\theta_{e'}$ is the lepton scattering angle measured w.r.t. the incoming proton direction and the electron and proton masses, m_e, m_p, have been neglected. For NC events the kinematic properties of DIS events can be determined either from the variables of the electron or of the final state hadron system, or from a mixture of both. For CC events only the hadron system is accessible for measurement.

From the electron:

$$Q_e^2 = 2 E_e E_{e'} (1 + \cos \theta_{e'}) \qquad y_e = 1 - (E_{e'}/E_e)(1 - \cos \theta_{e'})/2.$$

From the hadron system, using the method of Jacquet-Blondel[13] and summing the energies (E_h) , transverse (P_{Th}) and longitudinal momenta (P_{zh}) of all final state hadrons:

$$Q_{JB}^2 = \Sigma_h (P_{Th}^2)/(2\,E_e) \qquad y_{JB} = \Sigma_h (E_h - P_{zh})/(2\,E_e).$$

From the electron scattering angle and the angle γ_h which characterises the longitudinal and transverse momentum flow of the hadron system[14] (in the naive parton model γ_h is the scattering angle of the struck quark):

$$\cos\gamma_h = \frac{(\Sigma_h P_x)^2 + (\Sigma_h P_y)^2 - (\Sigma_h (E_h - P_{zh}))^2}{(\Sigma_h P_x)^2 + (\Sigma_h P_y)^2 + (\Sigma_h (E_h - P_{zh}))^2}$$

$$Q_{\gamma\theta}^2 = 4\,E_e^2 \sin\gamma_h (1 + \cos\theta_{e'}) / [\sin\gamma_h + \sin\theta_{e'} - \sin(\gamma_h + \theta_{e'})]$$

$$y_{\gamma\theta} = \sin\theta_{e'} (1 - \cos\gamma_h) / [\sin\gamma_h + \sin\theta_{e'} - \sin(\gamma_h + \theta_{e'})].$$

For NC events the precision of x, y and Q^2 can be improved by a simultaneous fit to all measured variables[15].

Table 2 compares the kinematic range accessible at HERA and in previous lepton - nucleon scattering experiment. The maximum energy transfer is increased by a factor of ~ 100: HERA is equivalent to a fixed target experiment with an incident electron beam of 52 TeV. The Q^2 domain over which lepton nucleon scattering can be measured is also increased by two orders of magnitude. Since the typical Q values in DIS are much larger than the proton mass the electron interacts with one of the partons (quarks, gluons, ..) rather than with the proton as a whole: HERA is in reality an electron - quark (or gluon) collider.

Table 2. Kinematic region accessible at HERA (E_e = 30 GeV, E_p = 820GeV) and in previous experiments

	HERA	pre - HERA
s (GeV^2)	10^5	10^3
maximum attainable Q^2 (GeV^2)	40 000	400
Δ (cm^{-1})	$1 . 10^{-16}$	$1 . 10^{-15}$
ν_{max} (GeV)	52 000	500
minimum x at Q^2 = 10 GeV^2	$1 . 10^{-4}$	$1 . 10^{-2}$

For the analysis of ep interactions at HERA an understanding of the event kinematics is helpful. It is complicated by the fact that the c.m. system is not at rest. The large momentum excess of proton over electron beam pushes most final state particles into the proton direction. The correlations between energy and angle of electron and current jet (ignoring gluon emission) are shown in fig. 22 in the x - Q^2 plane.

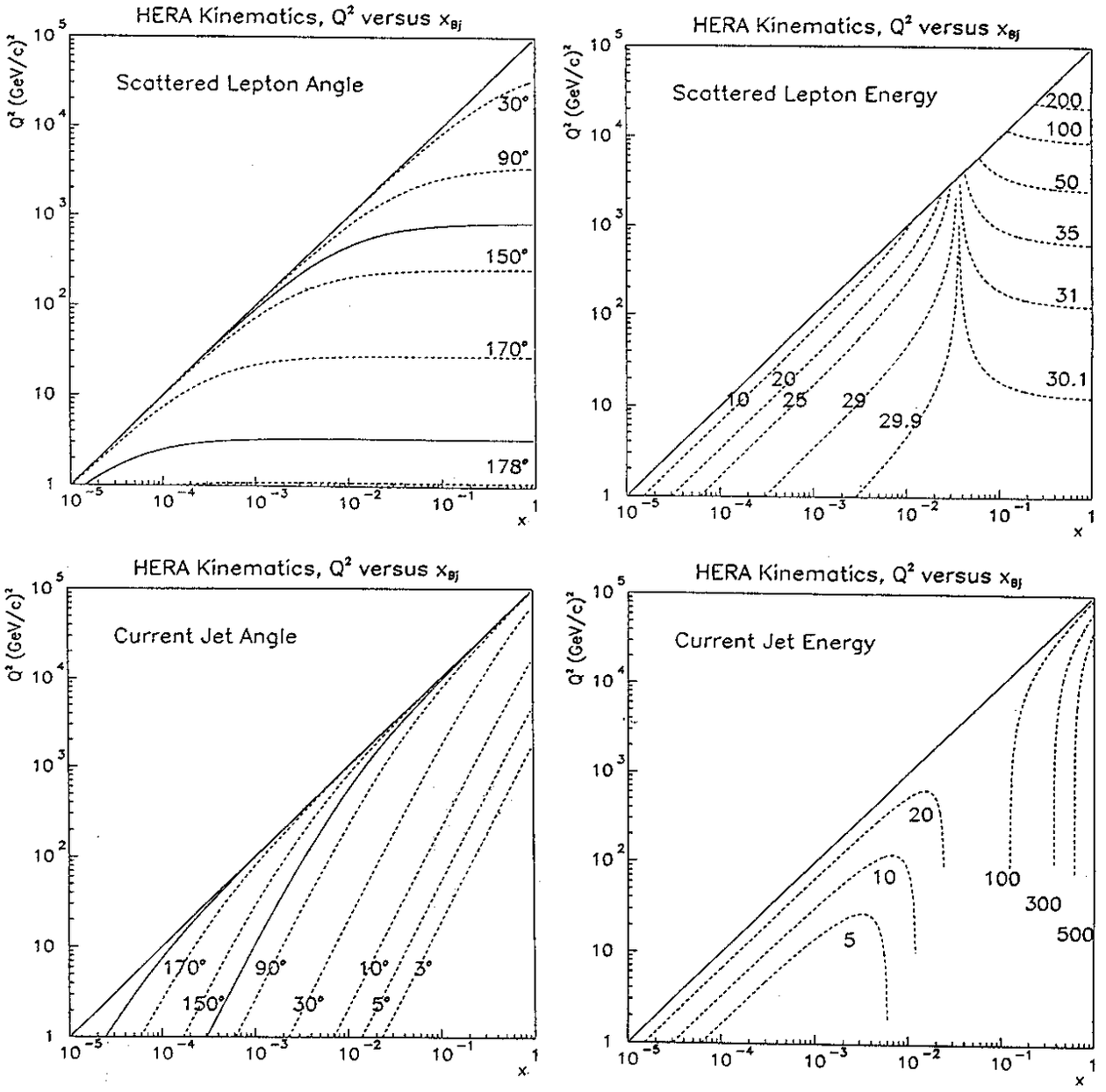

Fig. 22 The x - Q^2 dependence of the angle and energy of the scattered electron and the current jet (ignoring gluon radiation) for beam energies of E_e x E_p = 30 GeV x 820 GeV; the angles are measured w.r.t. the proton beam direction

5.1.2 Cross sections

The cross sections for NC and CC scattering are related to structure functions F_i of the proton:

NC, e p -> e X:

$$\frac{d^2\sigma(\gamma+Z^0)}{dx\,dy} = \frac{4\pi\alpha^2}{s\,x^2\,y^2}\,[(1 - y + y^2/2)\,F_2(x,Q^2) - y^2/2\,F_L(x,Q^2) \pm (y^2/2 - y)\cdot xF_3(x,Q^2)]$$

The upper (lower) sign applies to e^- (e^+) p scattering. For $Q^2 \gg 1$ GeV^2 and not too small x the contribution of the longitudinal structure function F_L is small (Callan - Gross relation[16]). The F_3 contribution arises from Z^0 exchange and is significant only when Q is comparable to the Z mass.

CC, e p -> ν X:

$$\frac{d^2\sigma\,(W)}{dx\,dy} = \frac{G_F^2\,s}{2\pi}\,\frac{1}{(1 + Q^2/M_W^2)^2}$$

$$\cdot\,[(1 - y + y^2/2)\cdot F_2(x,Q^2) \pm (y^2/2 - y)\cdot xF_3(x,Q^2)]$$

where G_F is the Fermi coupling constant, $G_F = 1.02 \cdot 10^{-5} / m_p^2$. As before, the upper (lower) sign applies to e^- (e^+)p scattering. The structure functions F_i from NC and CC scattering are in principle independent. They can be related via the quark parton model, however.

The structure functions measured in previous experiments have been extrapolated by QCD evolution[17] to the HERA regime (see fig. 23). The number of events expected from NC and CC scattering are shown in fig.24 for 500 pb^{-1}. The large NC rates at low Q^2 stem from photon exchange. At $Q^2 > M_Z^2$ contributions from Z - exchange become equally important. The requirement of a minimum of 100 events leads to a maximum Q^2 value of about 35 000 GeV^2 up to which NC measurements are feasible. The event rate for CC scattering at low Q^2 is much smaller. However, for Q^2 around M_Z^2 the CC and NC cross sections become equal (see fig. 25), i.e. weak and electromagnetic interactions are of the same strength. The practical Q^2 limit for CC studies is around 40 000 GeV^2.

5.1.3 Small x physics

Small x physics is a new and exciting field of lepton - nucleon scattering pioneered by Gribov, Levin and Ryskin[19]. The possibility of accessing this region at HERA has stimulated an intense discussion[20]. Since $x = Q^2/(2\,m_p\,\nu)$, small x - values are attained for fixed Q^2 by making the energy transfer ν large. At HERA, for $Q^2 = 10$ GeV^2, x - values as small as 10^{-4} can be reached which is a factor of 100

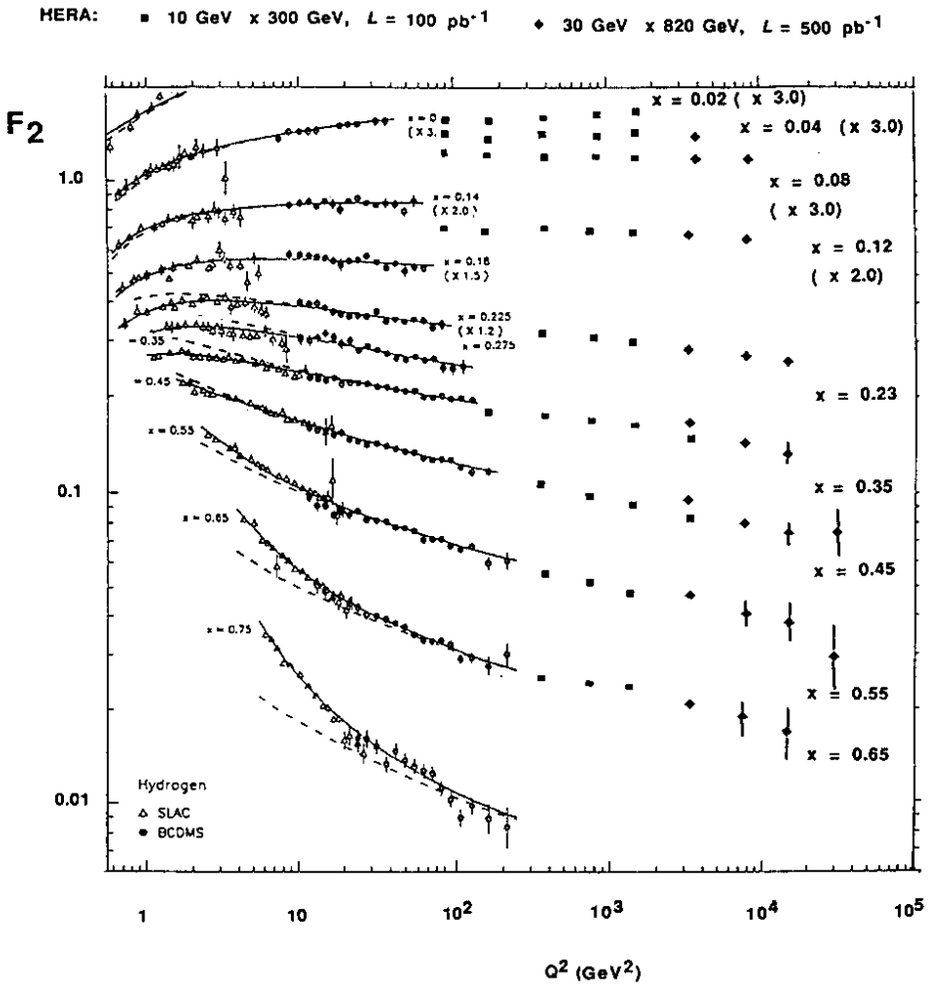

Fig. 23 The structure function F_2 for protons as measured by SLAC and BCDMS and as expected from HERA experiments at E_e x E_p = 30 GeV x 820 GeV with L = 500 nb^{-1}; the predictions for the HERA data have been taken from ref. 18

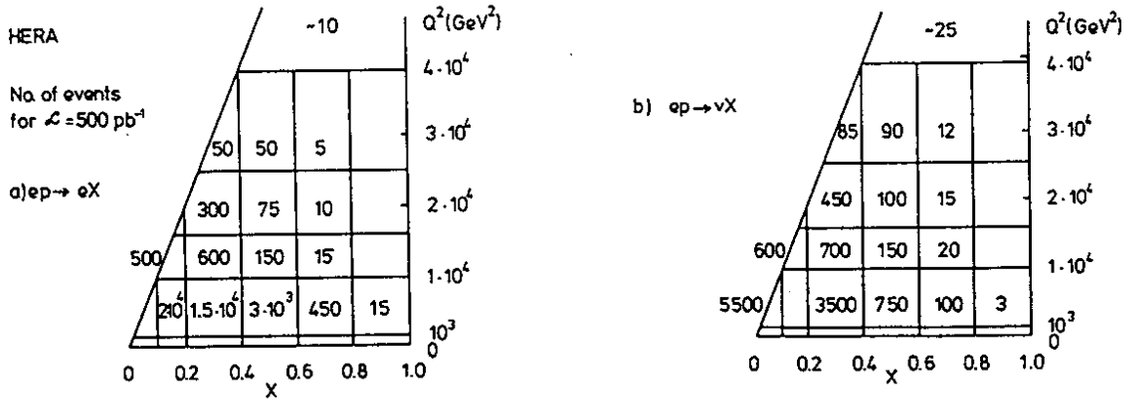

Fig. 24 Event rates for NC and CC scattering at HERA with L = 500 pb^{-1} calculated with LUND - LEPTO and EHLQ structure functions, and, the regions where x and Q^2 can be well measured at HERA for NC scattering from either the electron or the jet and for CC scattering only from the jet

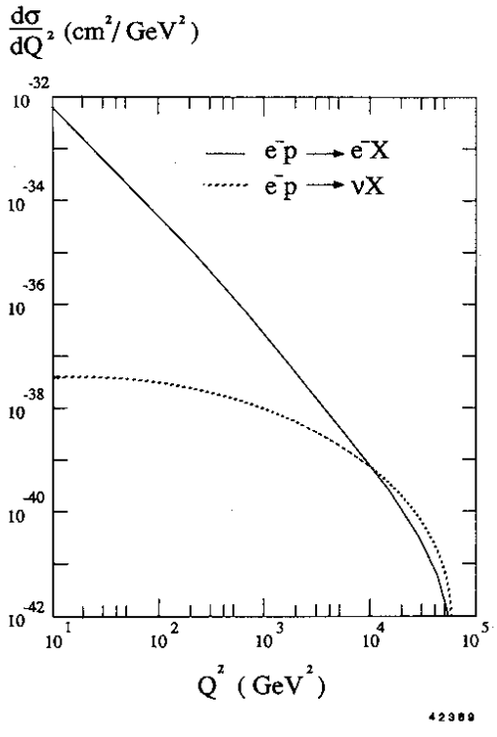

Fig. 25 The cross sections for NC and CC scattering as a function of Q^2

smaller than in previous experiments (see table 2). The NC cross section is favorably large in this regime as shown in fig. 26: for instance, the nominal yearly luminosity of 100 pb^{-1} should yield 10^6 events with $10^{-4} < x < 10^{-3}$, $10 < Q^2 < 20$ GeV^2.

Consider scattering (fig. 27a) at small x but not too small Q^2 such that α_s is small, e.g. $Q^2 > Q_0^2 = 10$ GeV^2. As $x \to 0$ the numbers of gluons and sea quarks in the proton are expected to grow beyond any limits (Regge picture), e.g. the number of gluons with momentum fractions x, x+dx should behave as $G(x) \sim x^{-3/2}$. Since the transverse size of the partons is fixed (~1/Q) and since the partons are confined to the proton and their number grows as $x \to 0$, there must be an $x = x_{crit}$ below which partons begin to overlap (fig. 28). This must lead to saturation of the structure functions as $x \to 0$ (fig. 29). A possible mechanism of parton overlap is depicted in fig. 27b : two ladders start from two different partons and begin to interact.

Two estimates for x_{crit} are given in fig. 30 as a function of Q^2 (from ref. 21). The first is characterized by a radius of 5 GeV^{-1} (proton radius) and assumes the parton distribution in the proton to be uniform. In this case the saturation region is barely within reach at HERA. For $Q^2 = 4$ GeV^2 the model predicts $x_{crit} = 10^{-4}$. However, the low - x partons may concentrate, for instance, around the valence quarks and form hot spots[22]. Assuming a hot spot radius of 2 GeV^{-1} observation of saturation effects at HERA looks feasible (fig. 30). The amount of saturation one may expect e.g. for the gluon structure function is shown in fig. 31 for the two models.

The smallest - x data for $Q^2 > 5$ GeV^2 that were presented before HERA were obtained by NMC[23]. Figure 32 shows their recent measurements of F_2 in μp scattering for x - values between 0.008 and 0.5. It is remarkable that the prediction for F_2 obtained by fitting previous data from higher x - values[24] fails to fit the NMC data: the NMC data indicate a faster rise of F_2 as x approaches zero. Inclusion of the new NMC data in the structure function fits has resulted in the predictions[25] D_0 and D_- shown in fig. 33. The two sets differ in the assumption on whether the gluon structure function is constant or diverges as x goes to zero: $xG(x,Q^2) \sim$ constant ($\sim x^{-0.5}$) for D_0 (D_-). While the two sets give identical results for $x > 0.01$ they make markedly different predictions for F_2 for $x < 10^{-3}$: at $x = 10^{-4}$ F_2 as calculated from D_- is a factor of three larger. Also indicated in fig. 33 is an estimate of the effects of parton saturation on D_-: they are small for a uniform proton but large in the hot spot model for $x = 10^{-4}$.

Deviations from the standard Altarelli - Parisi (GLAP) evolution at very small values of x are also expected for a "technical" reason. In the GLAP evolution for each additional factor of α_s only terms $\sim(\log Q^2)\cdot(\log 1/x)$ are kept while $(\log 1/x)$ terms are neglected. This approximation has been avoided in the Lipatov evolution[26].

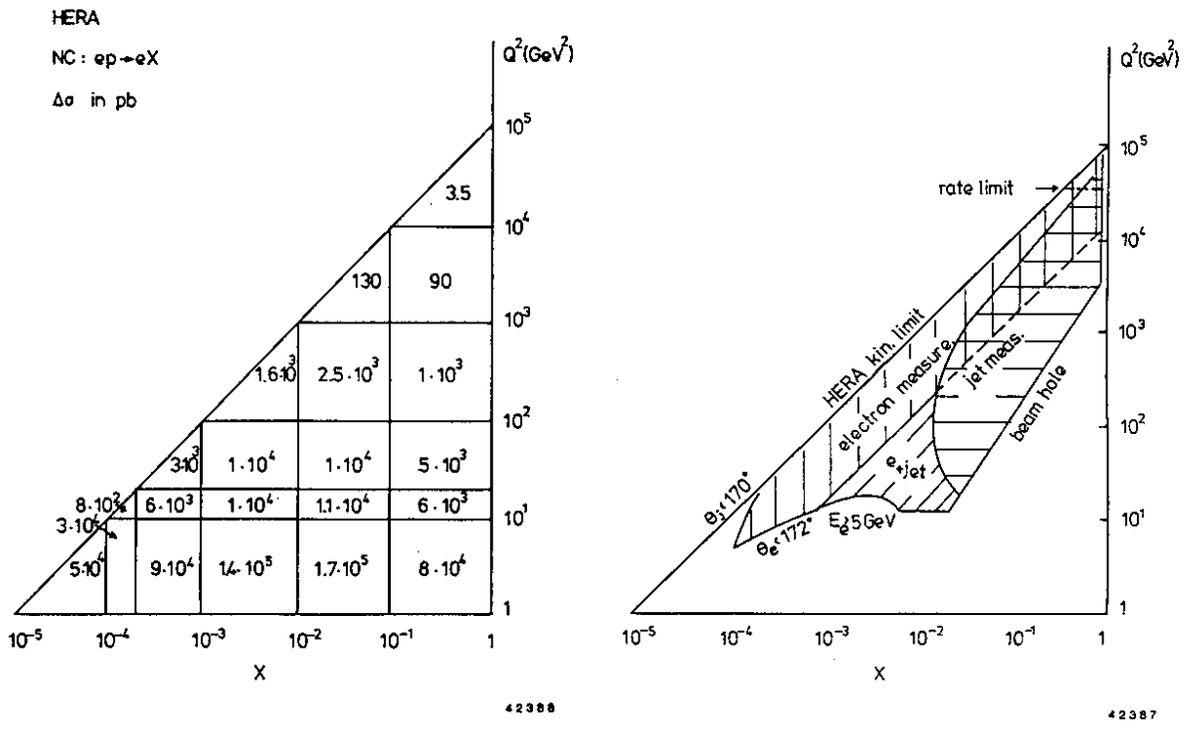

Fig. 26 a) The NC cross section at HERA for E_e x E_p = 30 GeV x 820 GeV calculated with LUND-LEPTO and EHLQ structure functions
b) The region where x and Q^2 can be well measured

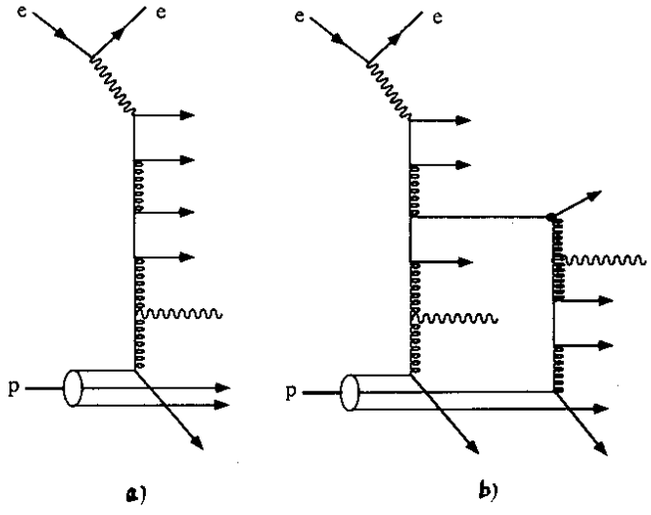

Fig. 27 Diagrams for low - x scattering: a) with a single ladder; b) with two ladders started from two different incoming partons and where the two ladders interact

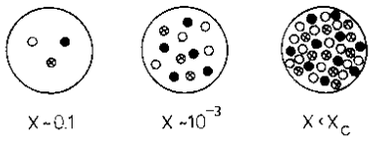

Fig. 28 The parton density in the nucleon for different values of x

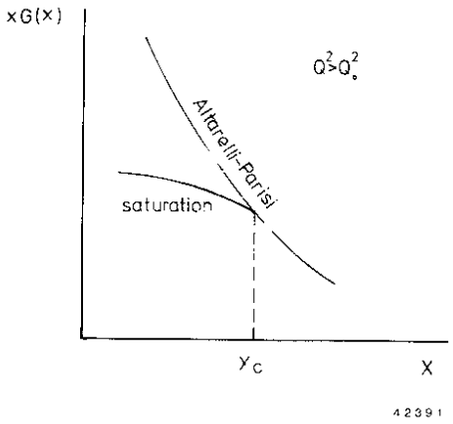

Fig. 29 Qualitative behavior of the gluon structure function at very small x values

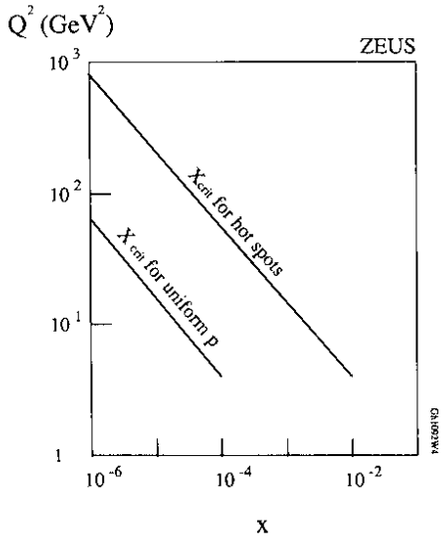

Fig. 30 Model predictions for the x - Q^2 behavior of x_{crit} for a uniformly populated proton (lower curve) and for the hot spot model (upper curve); from ref. 21

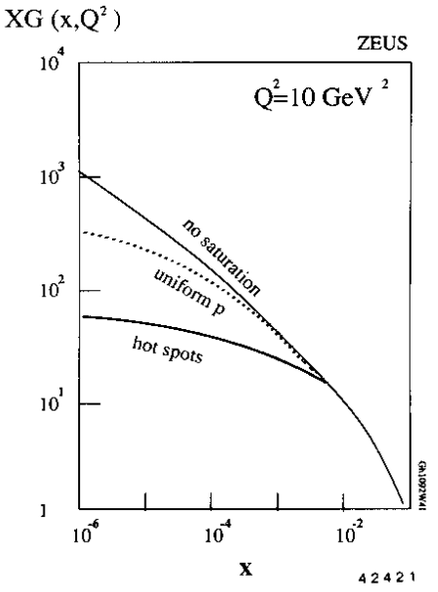

Fig. 31 Model predictions for the x behavior of the gluon structure function at Q^2 = 10 GeV^2 assuming no saturation or saturation for a uniformly populated proton and for the hotspot model; from ref. 21

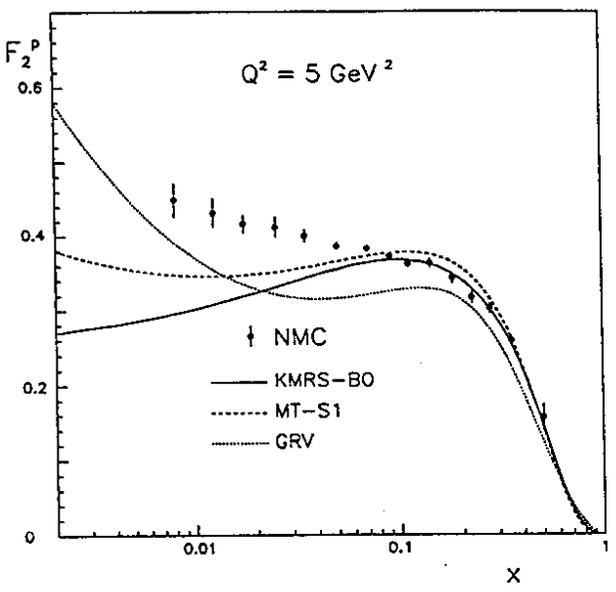

Fig. 32 The structure function F_2 as measured in μp scattering by NMC[23], together with predictions obtained from fits to previous DIS data[24]

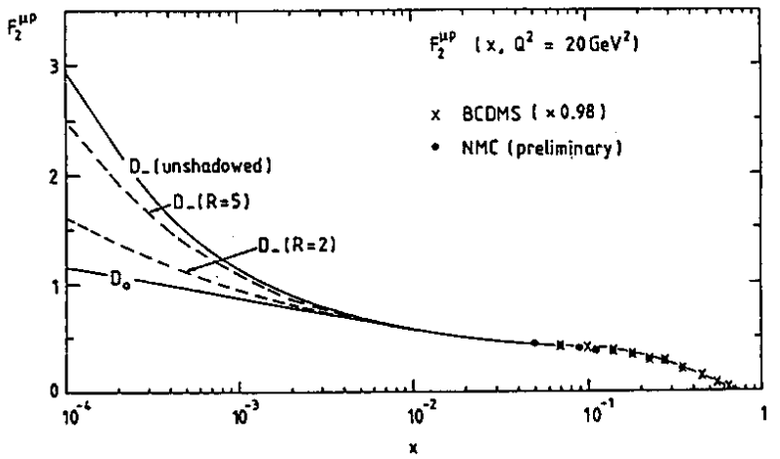

Fig. 33 Prediction for F_2 at very small x - values obtained from a fit [25] to the new data from NMC and other experiments assuming as x -> 0 : x G(x) ~ $x^{-0.5}$ (D_-) and x G(x) ~ constant (D_0)

5.1.4 Experimentally accessible x - Q2 region

Standard x - Q^2 region: The x - Q^2 region accessible to experiments depends on the structure of the events and on the detector. As discussed above, for NC events, the values of x and Q^2 can be determined from the energy and direction of *either* the scattered electron or the current jet. For CC events, where the scattered lepton is a neutrino, x and Q^2 can be measured only with the current jet. Figure 24b shows for nominal beam energies and standard x and Q^2 values the regions over which x and Q^2 can be measured well from the electron and the jet parameters, respectively. The main limitations stem from the precision with which the electron and jet energies can be measured, and from the size of the beam holes (see below). For NC scattering, structure function measurements should be feasible for basically the full range of x and Q^2. In the case of CC scattering precise measurements will be difficult for $y > 0.6$ and below $y \approx 0.02$. The well measurable region can be extended by operating HERA at smaller beam energies.

Small x - region: The major limitation for NC studies at very small x and low Q^2 values comes from the beam holes provided in the forward and rear calorimeters for beam passage. Typical cross sections of these holes are 20 x 20 cm^2 (ZEUS). The effective hole in the acceptance is somewhat larger since a reliable energy measurement requires the point at which electron or jet enter the calorimeter to be some distance away from the cutout. Figure 26b shows an educated guess for the well measurable region. It follows from the requirements

$$\Theta_{\text{current jet}} < 172^{\circ}, \quad \Theta_{\text{electron}} < 172^{\circ}, \quad E_{\text{electron}} > 5 \text{ GeV}$$

and from the size of the beam hole. The HERA experiments should be well suited for the region $x > 10^{-4}$, $Q^2 > 10$ GeV^2.

5.2 Results from H1 and ZEUS

For both experiments the prime goal in this first analysis was to establish that events from deep inelastic NC scattering can be isolated from background and have the expected characteristics and cross section. The description of the event selection will be rather sketchy; details can be found in refs. 27-29.

ZEUS analysis (ref. 27): Neutral current scattering was studied with an integrated luminosity of 2.2 nb^{-1}. The trigger selection was made by requiring energy deposition in the calorimeter and by making a loose timing cut. This led to a total of 1.10^6 accepted events.

The off-line analysis was also based on the calorimeter information. In the *preselection* energy deposition in the electromagnetic part of RCAL or BCAL, or an identified electron with energy > 4 GeV was required. An important variable that characterises the events is the difference between the total energy and longitudinal momentum measured in the calorimeter,

$$\delta = \Sigma_i (E - P_z)_i.$$

For ep events $\delta = 2 E_e$ if all final state particles are measured. Undetected particles which are emitted into the forward beampipe region give a negligible loss in δ since $E_i \approx P_{Zi}$. Initial state radiation moves events to lower δ values and measurement errors lead to a broadening of the δ distribution. Different final states produce different δ distributions, so that δ is a good discriminator against background processes. For instance, photoproduction events, in which the scattered electron escapes in the rear part of the beam pipe, will predominantly give low values of δ. Background events coming from interactions of the proton beam also have small values of δ. The distribution of δ is shown in fig. 34b. The preselected sample (open histogram) shows a broad shoulder near $\delta = 2 E_e$ superimposed on a large falling background.

The time distribution for events with energy deposition in FCAL and RCAL shows a clean separation between events from ep collisions and from background (fig. 34a). Therefore, the *final* selection was based on a tighter timing cut. It also required an electron with $E_e' > 5$ GeV and $35 \text{ GeV} < \delta < 60$ GeV. The vertex distribution along the beam for the *preselected* event shows a peak concentrated around $Z = 0$ on top of a large background (fig. 34c) while the events of the *final* sample (shaded distribution in fig. 34c) are basically background free. The background in the final sample from photoproduction was estimated at 2±1%.

The transverse momentum vectors of the electron, p_{Te}, and of the hadron system, p_{Th}, are back-to-back and of equal magnitude as expected for NC events (see fig. 35).

The variables x and Q^2 were determined from the angles of the electron (θ_e') and the hadron system (γ_h). In order to ensure that the current jet is sufficiently separated from the proton remnants and its direction measurable a cut of $y_{JB} > 0.02$ was introduced. The distribution of the events in the (x, Q^2) plane are shown in fig. 36. Most events lie in the Q^2 region between 5 and 100 GeV^2. In the x - direction the events populate mainly the region of very small x - values, $x < 10^{-2}$, with a sizeable number of events between $x = 10^{-3}$ and 10^{-4}. The projections of the data in x and Q^2 (fig. 37) are in reasonable agreement with Monte Carlo simulations performed with the set D_0 of ref. 25. The total cross sections, corrected for acceptance, measurement uncertainties and QED radiative effects, are shown in fig. 38. The data are consistent with all three structure function sets D_0, MTB1[30] (these two assume a constant gluon structure function, xG, as x -> 0) and MTB2[30] (diverging xG as x -> 0).

H1 analysis (ref. 28). NC candidates were selected from data corresponding to an integrated luminosity of 1.3 nb^{-1}. The trigger required a localized energy deposition or a cluster of more than 4 GeV in the BEMC calorimeter. Out-of-time events were rejected.

Off-line selection of DIS events from the 6.10^4 events accepted by the tigger

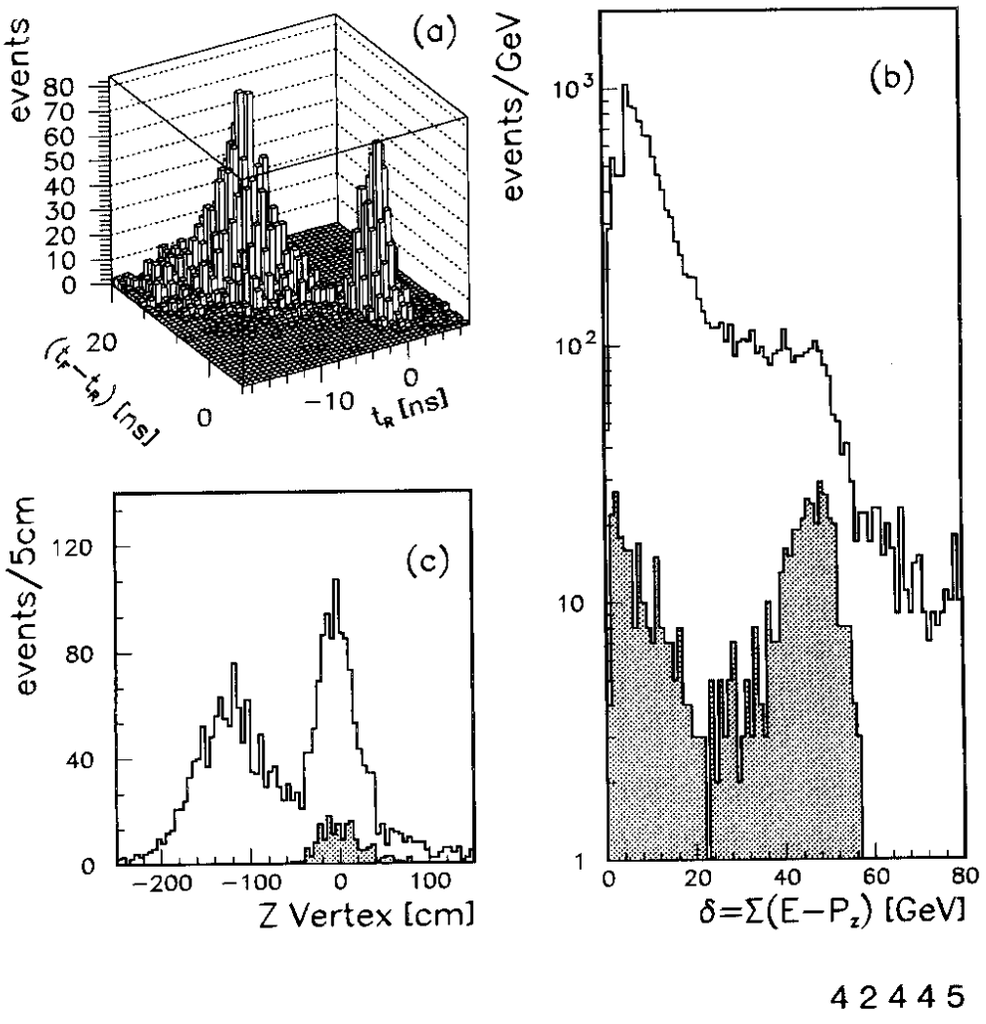

Fig. 34 a) Distribution of preselected events in (FCAL - RCAL) and RCAL times.
b) Distribution of $\delta = \Sigma_i (E - P_Z)_i$ at the preselection level. The shaded area shows the distribution after all cuts except that on δ itself.
c) The Z - distribution of event vertices at the preselection level. The shaded area shows the same for the final event sample with $y_{JB} > 0.02$.
From ZEUS

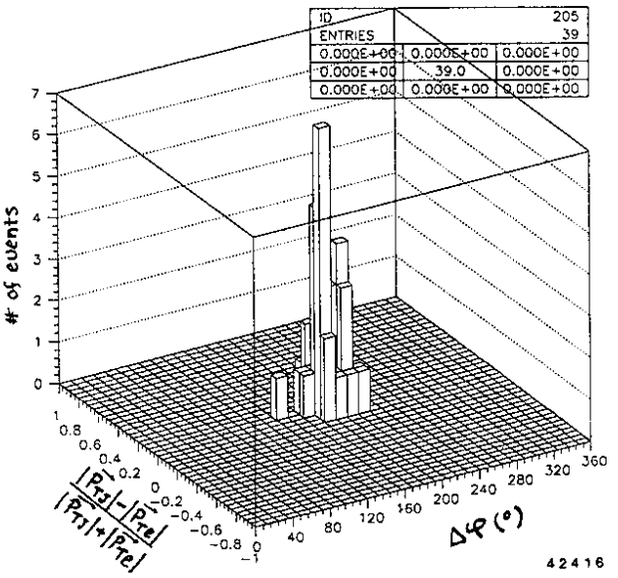

Fig. 35 Distribution of the nomalized difference of transverse momenta and azimuth angles of electron and jet for NC events from ZEUS with a scattered electron of $E_{e'} > 10$ GeV, $\theta_e < 172^0$ and a current jet of $E_{jet} > 15$ GeV

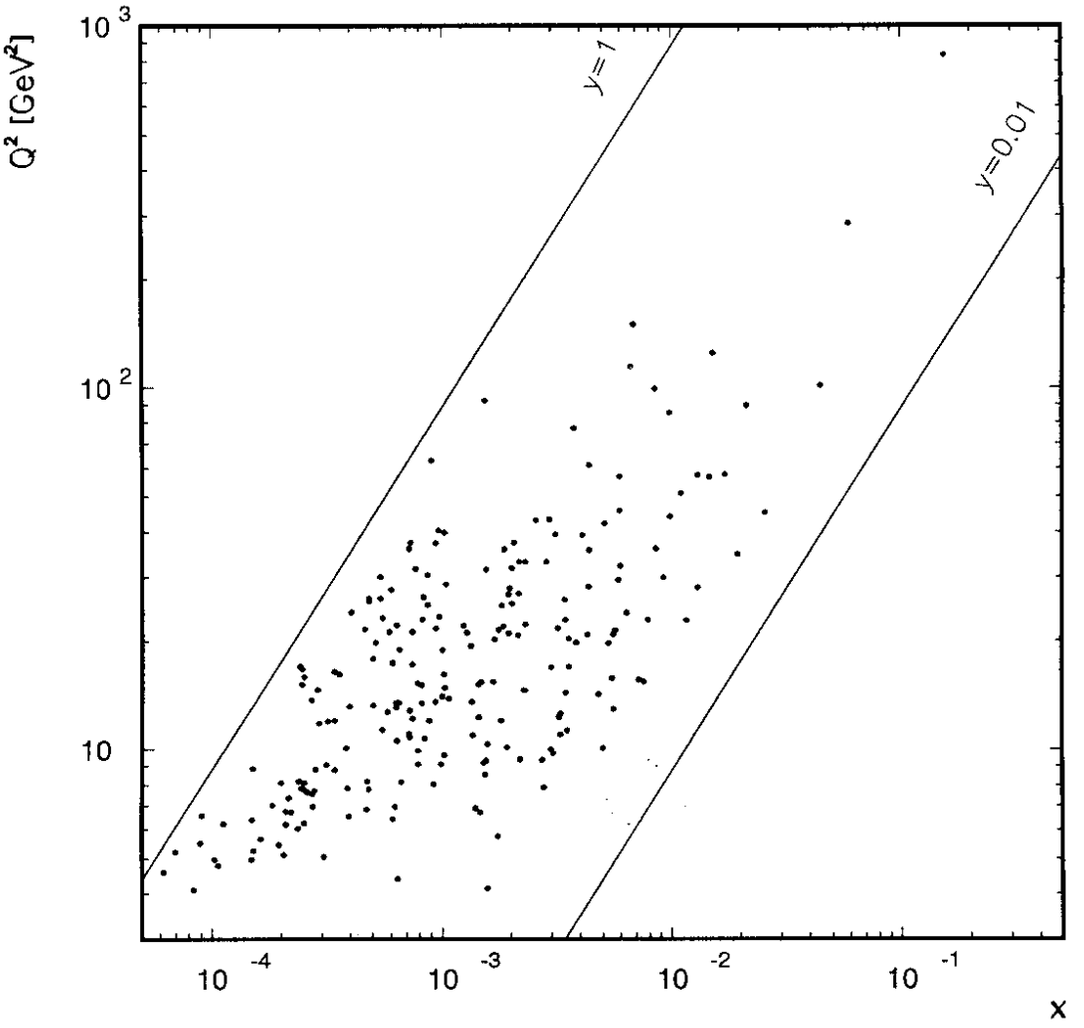

Fig. 36 The distribution of events in the x - Q^2 plane as measured by ZEUS

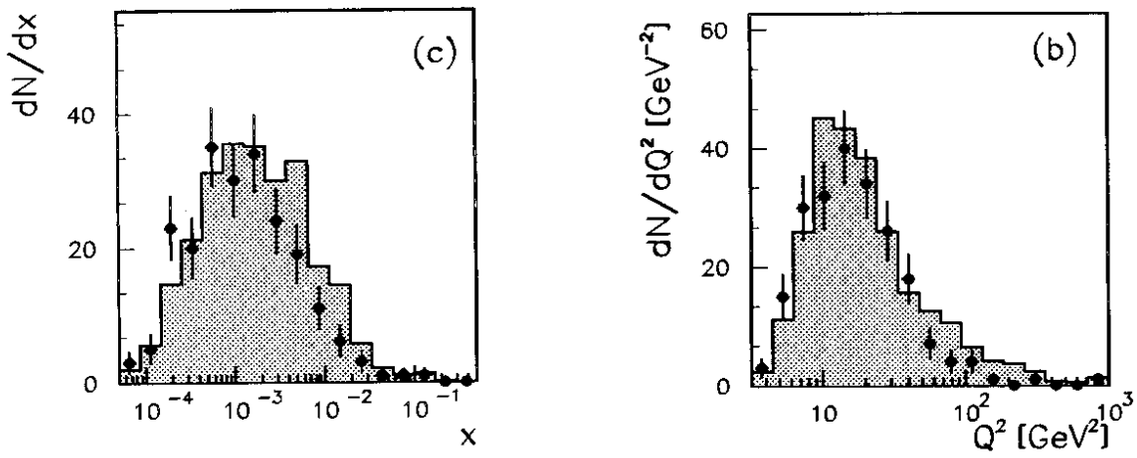

Fig. 37 The Q^2 and x distributions of the events as measured by ZEUS. The Monte Carlo predictions (shaded histograms) were calculated from the extrapolation of the MRSD0 parametrisation

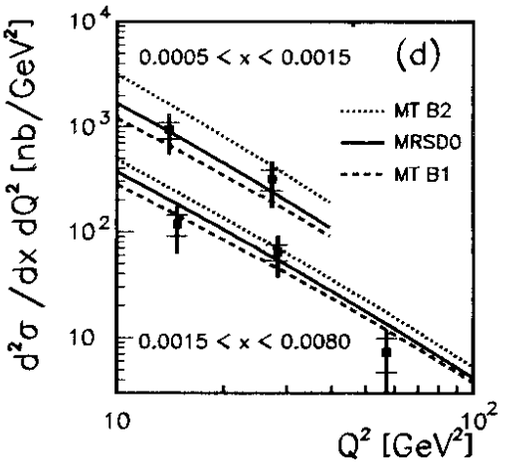

Fig. 38 The differential Born cross section in the x-Q^2 ranges indicated as measured by ZEUS. The lines show the extrapolations of the MTB1, MTB2 and MRSD0 parametrisations

was done by requiring a correlation between the BEMC cluster and hits from the tracking chambers and performing a vertex cut. In order to suppress further beam background and contributions from photoproduction, events with $y_e > 0.6$ and $y_{JB} < y_e/2$ were rejected. The energy spectrum of the scattered electron for the 148 accepted events is shown in fig. 39. The calorimeter was recalibrated by fitting the Monte Carlo prediction to the events with $E_e' > 22$ GeV. The background from photoproduction is estimated to be < 50% for $E_e' < 10$ GeV, < 20% for $10 < E_e' < 14$ GeV and negligible above; beam induced background is < 5% for $E_e' > 10$ GeV.

Cross sections were determined for $Q^2 > 5$ GeV^2, $0.025 < y_{JB} < 0.6$ and $\theta_e' < 174^\circ$ without radiative corrections as a function of x and Q^2 (fig. 40). The data agree broadly with the predictions from D_0, D_- and MTB1 but disfavor MTB2 somewhat.

H1 performed a first analysis of the final states of neutral current events[29]. Events were selected with $E_e' > 14$ GeV and hadronic c.m. energies squared $W^2 > 3000$ GeV^2. A total of 88 events were retained. Their average values $\langle Q^2 \rangle$ and $\langle W^2 \rangle$ were 15 GeV^2 and 10^4 GeV^2, respectively. The hadronic final states were studied using the information on charged tracks produced with polar angles $22^\circ < \theta < 160^\circ$ and transverse momenta (wrt. the beam direction) $p_T > 0.1$ GeV/c.

The results are summarized in figs. 41,42. The transverse energy flow of charged particles in terms of the pseudorapidity $\eta = -\log(\tan\theta/2)$ and the azimuthal angle ϕ wrt. the scattered electron in the plane transverse to the beams are shown in fig. 41. Here, all quantities were calculated in the lab. system. The sea - gull plot was determined in the hadronic c.m. system: fig. 42 shows the average transverse momentum squared as a function of Feynman $x_F = p_Z/p_Z(\max)$.

The data were compared with three different prescriptions for simulating QCD effects using for the soft parton fragmentation the Lund string model as implemented in JETSET (ref. 31). The three prescriptions are described briefly:

(a) Leading log parton showers (PS): parton cascades can start from the initial parton in the proton or from the scattered parton. The amount of gluon radiation depends on the scale of virtuality which can be chosen to be either Q^2 or W^2 (simulation denoted by PS(Q^2) or PS(W^2)), or a function of both. Since $\langle Q^2 \rangle$ is much smaller than $\langle W^2 \rangle$ in this experiment, PS(W^2) will predict much more gluon radiation than PS(Q^2). The simulation was performed with HERACLES (ref.32) for the electroweak interaction and LEPTO (ref.33) for the QCD processes.

(b) Color dipole model (CDM): Gluon emission is described by a chain of radiating color dipoles between the scattered parton and the proton remnant. As implemented in ARIADNE (ref. 34), the virtuality scale is given by the p_T^2 of the radiated gluon and its maximum is proportional to $W^{4/3}$.

(c) $O(\alpha_s)$ matrix element and parton showers (ME + PS): Exact $O(\alpha_s)$ matrix

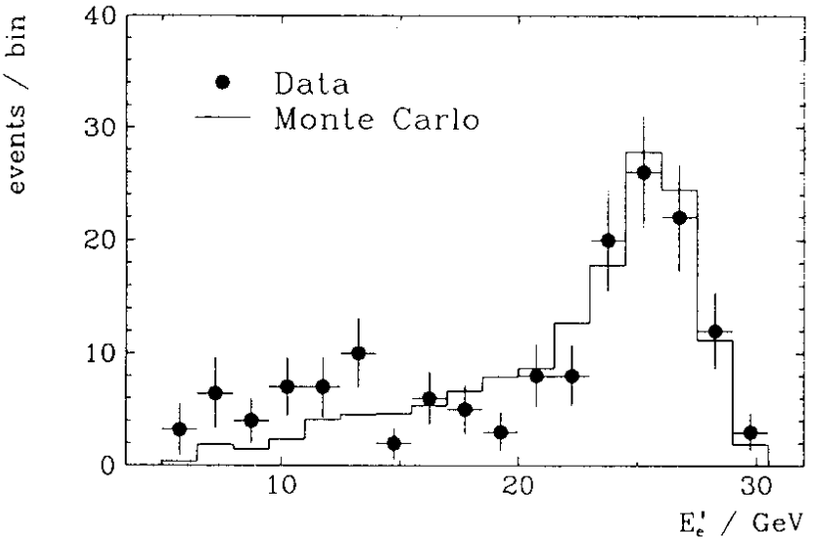

Fig. 39 Electron energy distribution for NC candidate events of H1 compared with the prediction for the MRSD0 parametrisation

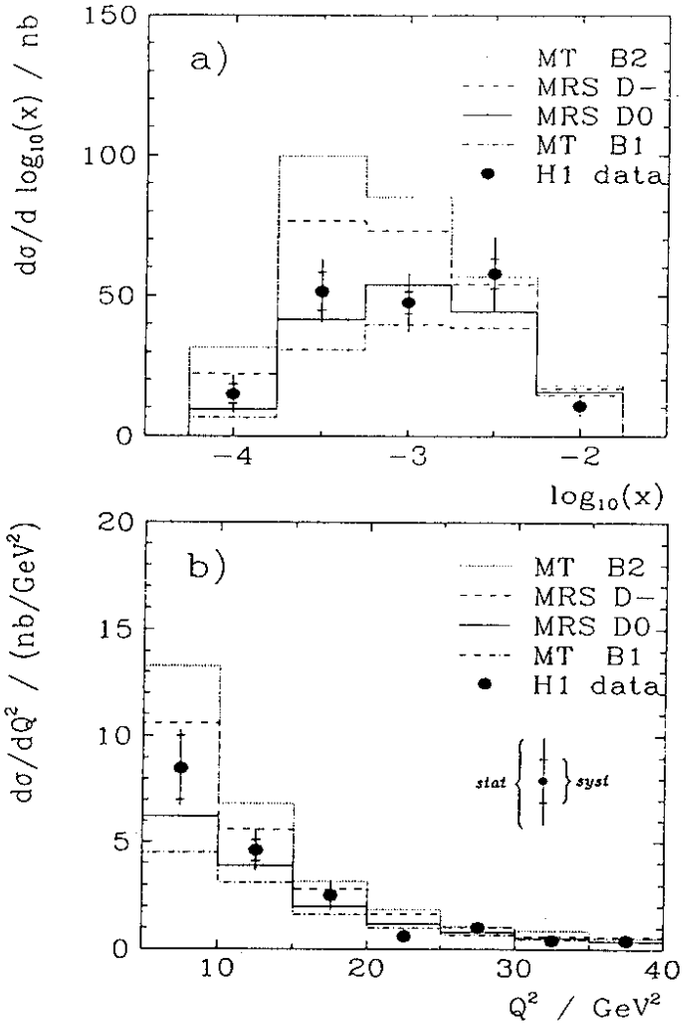

Fig. 40 Differential cross sections in log x and Q^2 in the range $0.6 > y > 0.025$, $Q^2 > 5$ GeV^2 and $\Theta_e < 174^o$ as measured by H1. The cross sections are not corrected for radiative effects. The full error bars correspond to the statistical errors; the smaller systematic errors are also indicated.The lines show cross section calculations for different parton density parametrizations.

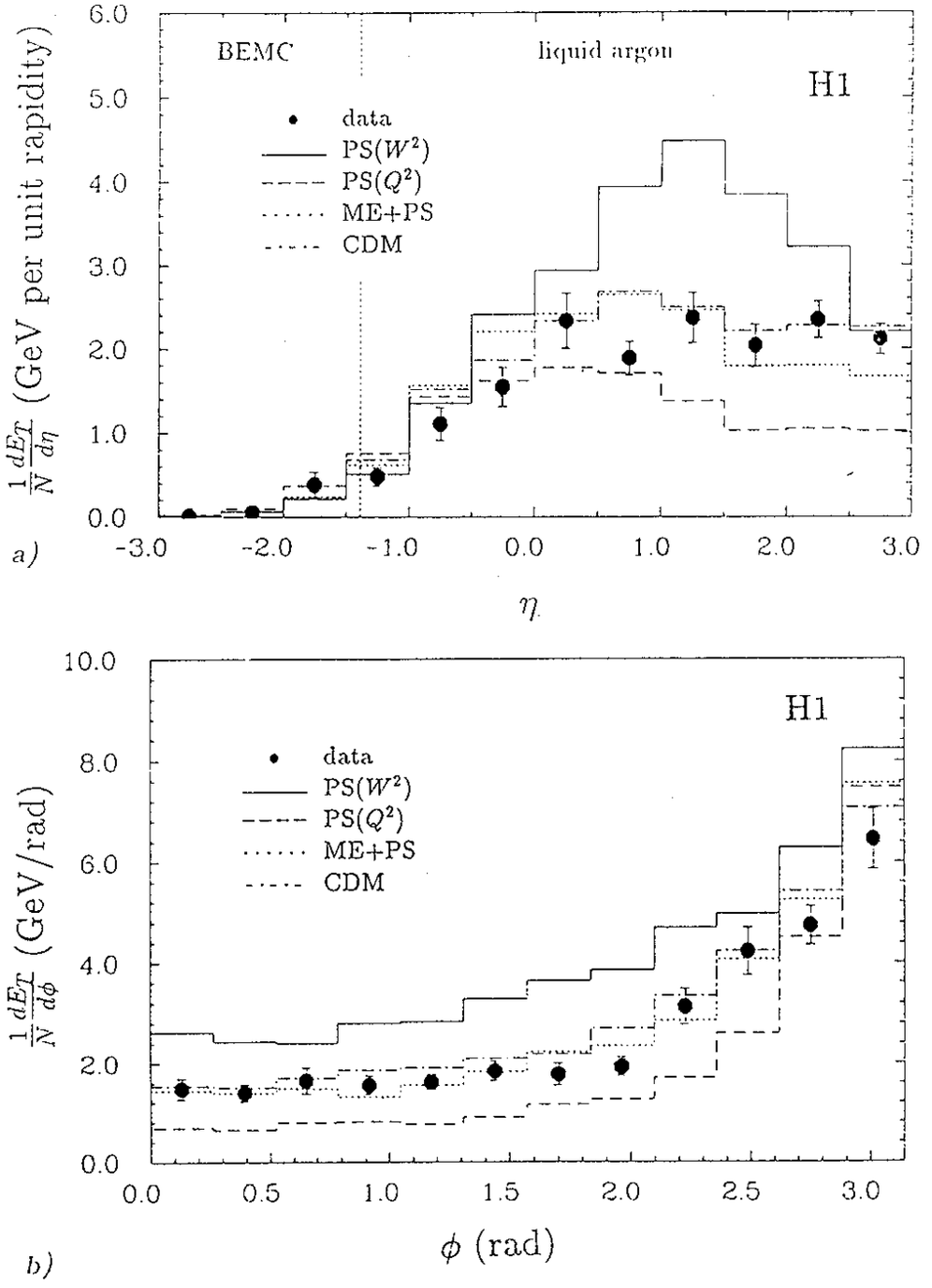

Fig. 41 Transverse energy flow E_T in the laboratory frame as a function of (a) pseudorapidity and (b) of the azimuthal angle with respect to the scattered electron direction in the plane transverse to the beam direction. The model predictions are also shown. From H1

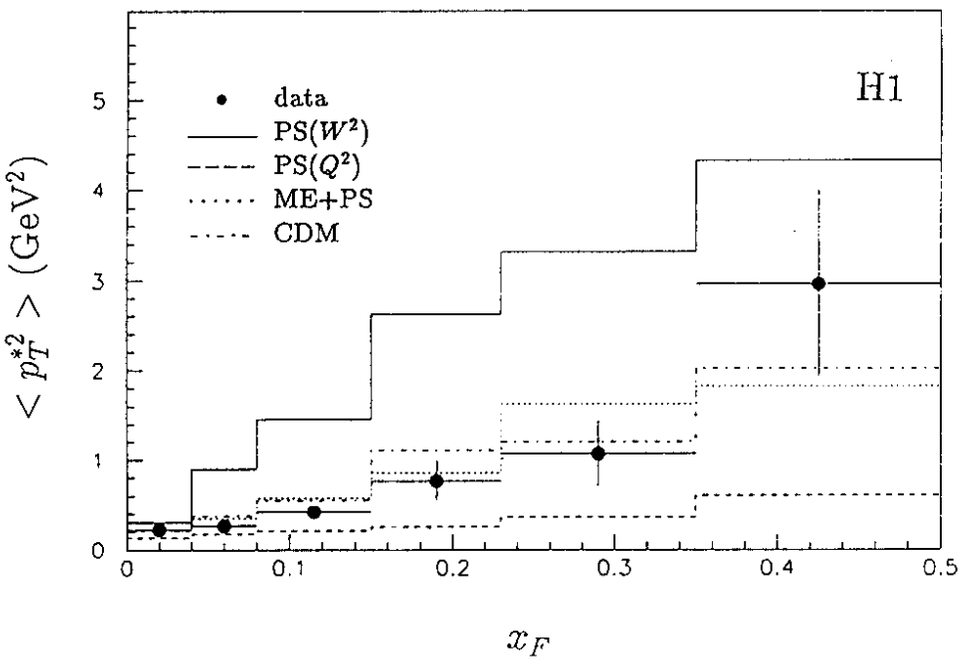

Fig. 42 Distribution of the average transverse momentum squared as a function of Feynman $x_F = p_z/p_z(\max)$ in the hadronic c.m. system, as measured by H1

elements are used for simulating the gluon radiation and photon gluon fusion processes while softer gluon emissions are added using the parton shower model. Using LEPTO (ref. 33) the maximum virtuality is related to the first order matrix element.

The comparison of the data with these models shows that CDM and ME + PS reproduce the measured results well while the leading log model fails if either Q^2 or W^2 is chosen as the scale of virtuality.

6. LEPTOQUARKS

Leptoquarks (LQ) are expected in many models. Production of leptoquarks in e - p collisions can proceed in several ways depending on the couplings and the leptoquark mass. The most favorable process for HERA is s - channel production(fig. 43): the electron with energy E_e and a quark with energy $x \cdot E_p$ form a leptoquark of mass squared $M_{LQ}^2 = 4 \times E_e E_p = xs$.

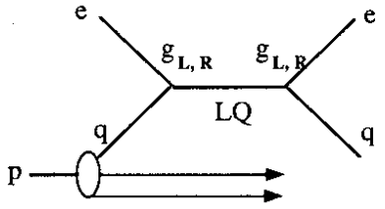

Fig. 43 Diagram for leptoquark production

In the x - Q^2 distribution leptoquark production will populate a narrow band with fixed x. For narrow leptoquarks, the production cross section and the branching ratio into electron + X are given by[36]

$$\sigma_{LQ} = \pi/(4s) \cdot (g_L^2 + g_R^2) \cdot u(x = M_{LQ}^2/s)$$
$$BR(LQ \rightarrow e + u) = (g_L^2 + g_R^2) / (2 g_L^2 + g_R^2)$$

where g_L and g_R are the left and right handed coupling constants and u(x) is the u-quark density in the proton. The coupling strengths are unknown. For g = 0.3 the coupling would have the same strength as the electromagnetic coupling, $g^2/4\pi = \alpha$.

The x - Q^2 distributions measured by H1 and ZEUS show no evidence for a leptoquark signal which is not surprising in view of the small luminosity of ~ 1 - 2 nb^{-1}. The data exclude LQ with masses of 30 - 50 GeV for g = 0.3 (Refs. 6,7,37). A run with 1 pb^{-1}, which is the nominal luminosity per day, will extend the mass range up to ~ 200 GeV.

7. TOTAL PHOTOPRODUCTION CROSS SECTION

7.1 Physics Introduction

For nonafficionados a measurement of the total photoproduction cross section, $\sigma_{tot}(\gamma p)$, at high energies may seem rather dull. A closer look at the underlying physics, however, shows that the subject has very interesting aspects. It has recently been reviewed by G. Schuler[38] and the following discussion draws heavily on his report.

Next to $p\bar{p}$ interactions, γp scattering is the only other hadronic or hadron - like reaction for which the total cross section can currently be measured at c.m. energies of several hundreds of GeV. In the VDM picture the photon couples to vector mesons V (ρ, ω, ϕ ..) which in turn interact with the proton. As a result $\sigma_{tot}(\gamma p)$ is related to the cross sections for Vp, and via the quark - parton model, for $\pi^{\pm}p$ and $K^{\pm}p$ scattering. Like the purely hadronic reactions, $\sigma_{tot}(\gamma p)$ in this model has three pieces coming from pomeron exchange, nonpomeron exchange and from partonic scattering in hadron - hadron interactions (fig. 44a-d). The behavior of $\sigma_{tot}(\gamma p)$ at high energies is therefore expected to be very similar to that of $\sigma_{tot}(p\bar{p})$ (although the hard scattering part of Vp is presumably larger than for pp due to a harder x - distribution of quarks).

The photon, in addition to its hadronic features, however, possesses a property which makes it distinctly different from hadrons: it couples directly to quarks and the coupling is pointlike. This leads to additional hard scattering processes which become prominent at high energies and which are not present in hadron - hadron interactions. They are represented by two types of diagrams: the first ("direct photon process") results from photon - gluon fusion into a quark - antiquark pair (fig. 45a) and from photon scattering off a quark in the proton under the emission of a gluon ("QCD Compton process"), see fig. 45b. But the quarks coupling to the photon can also emit gluons (e.g. fig. 45c), and either a quark or a gluon may participate in the hard scattering(fig. 45d,e). Together with the hard scattering of the hadronic (VDM) photon the hard scattering due to the anomalous quark and gluon content of the photon constitute the "resolved photon processes". They are summed in the photon structure functions F^{γ} which describe the quark and gluon content of the photon (note: part if not all of the hard scattering contributions from VDM and from the anomalous quark and gluon content of the photon are presumably identical and care must be taken to avoid double counting). The hard photon processes - direct or resolved - give rise to quark and gluon jets (sometimes called "minijets") with large transverse momenta. Their cross sections have been calculated and found to depend critically on the minimum momentum transfer p_{Tmin} down to which the integration is performed. As will be seen below, at HERA energies hard scattering originating from photon constituents is clearly visible.

The behavior of $\sigma_{tot}(\gamma p)$ at high energies is closely linked to the density of

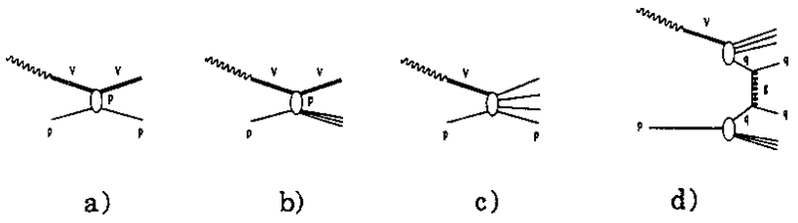

Fig. 44 Diagrams for photoproduction via VDM of vectormesons V by elastic (a) and inelastic diffractive scattering (b), for photoproduction via VDM by nondiffractive processes (c) and hard scattering (d)

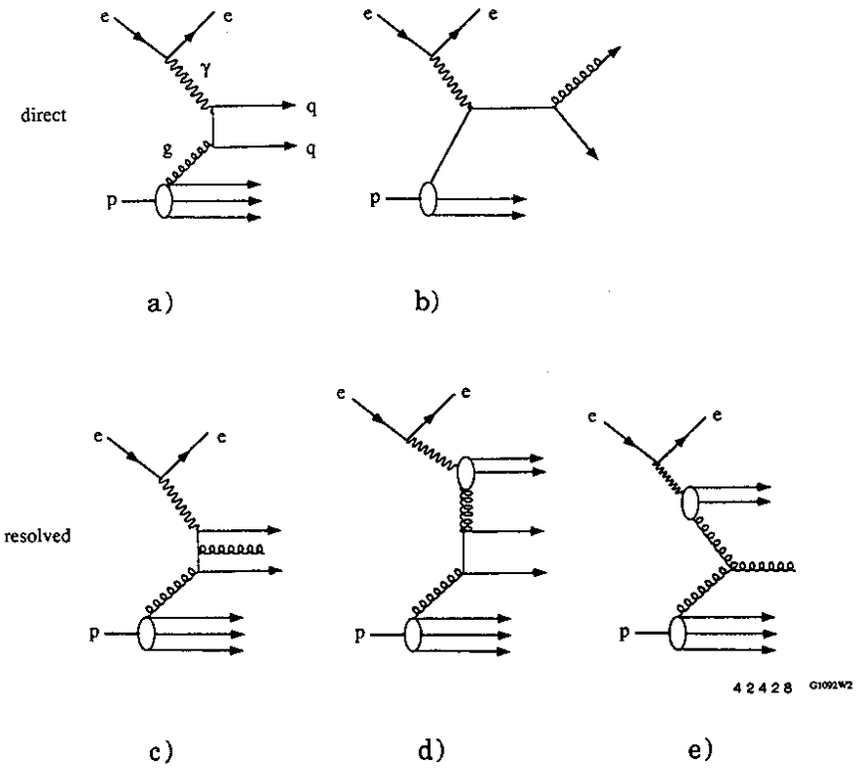

Fig. 45 Diagrams for direct (a,b) and resolved photon processes (c -e)

soft or low - x partons in the proton. The relation between the proton structure function F_2 and the total transverse and longitudinal photon proton cross sections is given by

$$F_2(x, Q^2) = \frac{(1-x)\,\nu^2 Q^2}{4\pi^2 \alpha\,(Q^2+\nu^2)}\,(\sigma_{trans} + \sigma_{long})$$

where ν is the photon energy for a stationary proton. As $Q^2 \to 0$: $\sigma_{long} << \sigma_{trans} = \sigma_{tot}(\gamma p)$. For small $x << 1$ and high energies, $\nu^2 >> Q^2$, the result for $Q^2 \to 0$ is:

$$F_2(x, Q^2) \approx \frac{Q^2}{4\pi^2\alpha}\,\sigma_{tot}(\gamma p).$$

Under the assumption that for very small x and Q^2 F_2 is of the form

$$F_2(x, Q^2) \sim x^{-\gamma}\,(Q^2)^{\delta}$$

it follows that

$$F_2(x, Q^2) \sim (Q^2)^{-\gamma+\delta}\,(2m_p\,\nu)^{\gamma} \approx (Q^2)^{-\gamma+\delta}\,W^{2\gamma}$$

where W is the total γp c.m. energy. Continuity for F_2 is preserved as $Q^2 \to 0$ if $F_2 \sim Q^2$ and therefore

$$\sigma_{tot}(\gamma p) \sim W^{2\gamma}.$$

The energy dependence of the total cross section at high energies is driven by the parton density of the proton at low x.

The definition for F_2 used here is the standard one, given in sect. 5.1.2. A "microscopic" treatment might separate F_2 into a term describing the "proton proper" (whatever this is) and a term due to resolved photons. In this case F_2 is expected to be dominated by the x distribution of the gluon in the resolved photon structure function[38].

Observations of "diffractive" air showers[39] and an excess of muons in very energetic cosmic air showers[40] have suggested $\sigma_{tot}(\gamma p)$ to rise much faster than $\sigma_{tot}(p\bar{p})$ at beam energies above ~ 100 TeV. This rise has been attributed to the semi-hard scattering arising from the resolved photon contributions. Since gluon initiated processes dominate, the rise is driven by the x-dependence of the gluon

distribution for photons and protons[41].

7.2 H1 and ZEUS Results

Photoproduction at HERA is part of neutral current scattering, ep -> eX, with the exchanged photon being almost real, $Q^2 \approx 0$. For events of this type the electron is scattered in the direction of the electron beam. It can be tagged in the electron calorimeter of the luminosity monitor (fig. 8) and its energy, E_e', measured. This determines the energy k of the exchanged photon in the HERA system, $k = E_e - E_e'$, and the photon proton c.m. energy W, $W^2 = 4\,k\,E_p$. For a minimum energy of the scattered electron of 4 GeV c.m. energies up to 300 GeV can be measured at HERA which is equivalent to a photon of energy $\nu = W^2/(2m_p)$ $\approx$ 47 TeV striking a stationary proton.

Since the standard DIS trigger of ZEUS had an acceptance of only 4% for photoproduction events a special run was performed with reduced energy thresholds of the calorimeter trigger[42]. Data were taken over a period of 7 hours of running yielding a total luminosity of 233 μb^{-1} and 53k events. The main requirements for photoproduction events were an electron tagged in LUMI (scattering angle < 6 mrad), a minimum energy of 1.1 GeV in the rear calorimeter (RCAL) and proper calorimeter timing. In total 212 events satisfied these conditions of which 182 were accepted after a visual scan. The event vertex was reconstructed from the tracking information for 72% of the events. The vertex position peaks close to the origin in contrast to the uniform distribution characteristic of beam gas events (fig. 46). For the final sample of 97 events the energy of the scattered electron was required to lie in the range 10 - 16 GeV (W = 186 - 233 GeV) resulting in maximum and average Q^2 values of 0.02 and 0.0006 GeV^2, respectively. Hence the contribution from longitudinal photons can safely be neglected and the measured process is scattering of (almost) real photons on protons.

The main difficulty in the extraction of $\sigma_{tot}(\gamma p)$ lies in the fact that the trigger acceptance A depends strongly on the type of process. It is low for the "elastic" reaction $\gamma p \to \rho p$ (fig. 44a) and sensitive to the details of the model, A = 10 - 27%. For these events the proton disappears mostly undetected in the forward direction and the $\pi^{\pm}$ from ρ decay escape often unseen in the backward direction. For inelastic diffractive processes (fig. 44b) A = 40 - 50% while for low - p_t reactions (fig. 44c) A = 70%; for hard processes such as direct and resolved photon contributions A = 80%. The final acceptance calculation was made assuming 20% from elastic plus diffractive processes and 80% from low p_t processes. The resulting predictions for the energy spectra seen in the three sections of the calorimeter give a reasonable description of the data (fig. 47). One point is particularly noteworthy: the data show 18 events with zero energy deposition in the FCAL. These events are candidates for the elastic and inelastic diffractive processes. The Monte Carlo predicts 16 events, in good agreement with the data.

The photoproduction candidates in the H1 experiment were obtained mainly by requiring a tagged electron (E_e' = 10 - 19 GeV) and a track in the central tracking detector pointing to the vertex region[43]. Most of the remaining

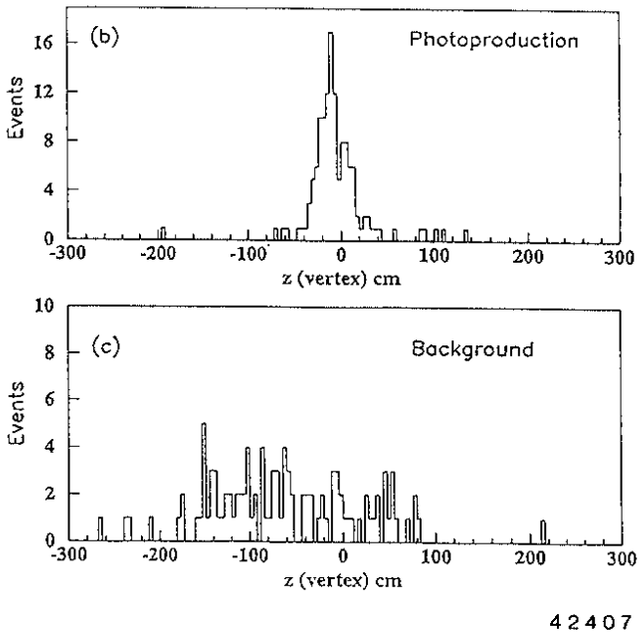

Fig. 46 Distribution of the vertex coordinate along the beam for ZEUS events from photoproduction (top) and beam - gas interactions (bottom)

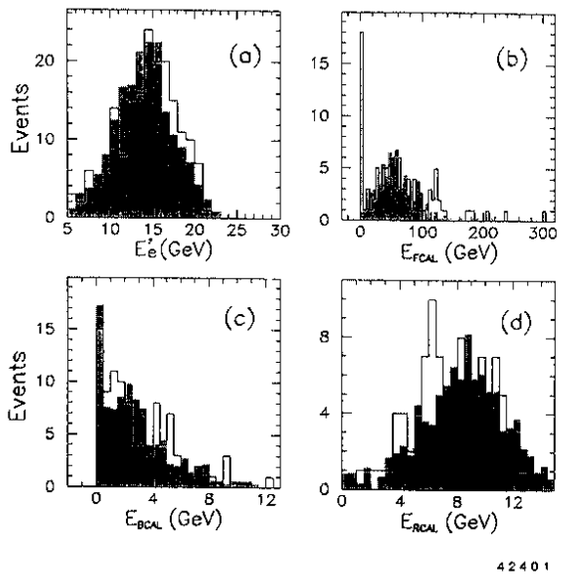

Fig. 47 Photoproduction data from ZEUS:
(a) The energy distribution of the scattered electron as measured by LUMI;
(b) - (d) The energy deposited in FCAL, BCAL and RCAL for photoproduction

background was due to proton gas interactions. It was statistically subtracted using the energy spectrum of the tagged electron which is substantially different for the signal and background events (fig. 48). The final sample consisted of 917 ± 38 events from a luminosity of 1.5 μb^{-1}. The acceptance was calculated assuming 26% elastic plus inelastic diffractive events, 55% low p_t and 19% hard scattering events as suggested by an extrapolation of low - energy photoproduction data.

The total cross section values obtained by the two experiments are

$$\sigma_{tot}(\gamma p) = 159 \pm 7\,(stat) \pm 20\,(syst)\,\mu b \quad \langle W \rangle = 195\ GeV,\ H1$$
$$154 \pm 16\,(stat) \pm 32\,(syst)\,\mu b \quad \langle W \rangle = 210\ GeV,\ ZEUS$$

Radiative corrections were calculated to be small. For H1 they increase the measured cross section by to $2.4\%^{+1.4}_{-2.5}\%$; the cross section was corrected accordingly. For ZEUS the corresponding increase is 1%. The systematic errors reflect the uncertainties in the determination of the acceptance and the luminosity.

Figure 49 shows $\sigma_{tot}(\gamma p)$ as a function of W above the resonance region (W> 1.75 GeV) as measured in previous experiments up to W = 18 GeV [44] and by H1 and ZEUS. No dramatic rise is observed between 18 and 200 GeV.

The curve labelled DL in fig. 49 is the prediction of a Regge - type fit to hadronic and pre - HERA photon proton total cross sections of the form

$$\sigma_{tot} = X s^{\epsilon} + Y s^{-\eta}$$

where the first term describes Pomeron contributions and the second one those from ρ, ω, f, a exchange[45]. The values of ϵ, η were obtained from fits to pp and $\bar{p}p$ data alone yielding $\epsilon = 0.0808$ and $\eta = 0.4525$ while the coefficients X, Y were determined from fitting the low energy data on $\sigma_{tot}(\gamma p)$. The curve ALLM is also based on a Regge-type analyse using the low energy photoproduction measurements together with proton structure function data[46]. Both predictions agree rather well with the HERA measurements.

The other curves shown in fig. 49 are based on the assumption that the total cross section is a sum of a soft part plus the contributions from the direct and resolved photons[47]. They depend critically on the choice of photon structure function F^{γ} and on the parameter p_{Tmin} which is the lower integration limit for the hard processes. Here, p_T is the transverse momentum cutoff in the c.m. system of the hard subprocess. The dashed - dotted lines use the parametrization of F^{γ} from ref. 48 with p_{Tmin} = 2.0 GeV/c for the lower (1.4 GeV/c for the upper) line. The dashed (dotted) line uses F^{γ} from ref. 49 and p_{Tmin} = 2.0 (1.4 GeV/c). A critical appraisal of the different calculations can be found in ref. 50. Only the dashed - dotted curve - which makes the lowest cross section prediction - is in agreement

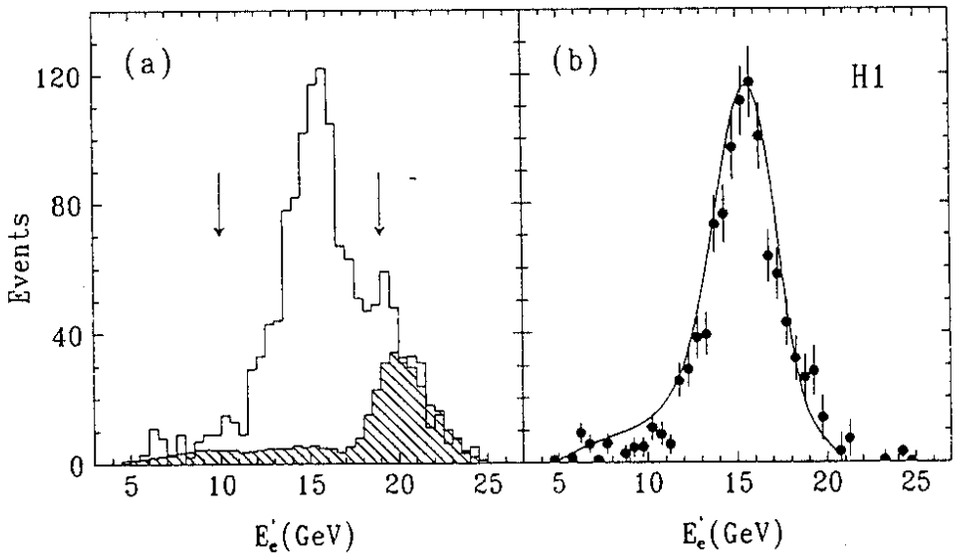

Fig. 48 Energy spectrum from H1 of tagged electrons for background events from the unpaired electron bunch (left) and for tagged events (right), compared with the tagger acceptance (curves)

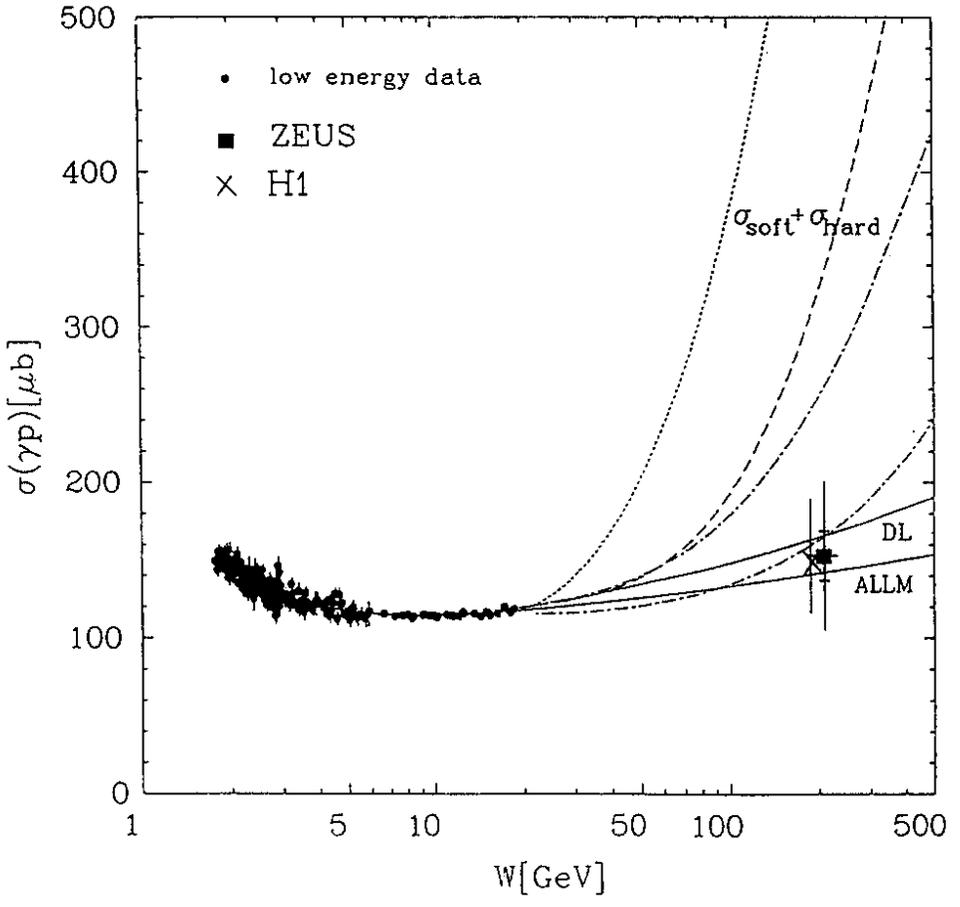

Fig. 49 The total γp cross section as a function of the c.m. energy W as measured below 18 GeV and by H1 and ZEUS near W = 200 GeV. The lower solid curve is the prediction of the ALLM[46] parametrization and the higher solid curve is that of DL[45]. The dotted (dashed) line uses the LAC1 parametrization[49] for the photon with p_{Tmin} = 1.4 GeV/c (2 GeV/c). The dash-dotted lines use the DG parametrization for the photon[48] with p_{Tmin} = 1.4 GeV/c (upper line) and p_{Tmin} = 2 GeV/c (lower).

with the HERA data. A strong rise of $\sigma_{tot}(\gamma p)$ that might have been expected in the HERA regime from the cosmic ray results and/or from direct and resolved photon contributions is postponed to higher energies, if at all.

8. HARD SCATTERING IN PHOTOPRODUCTION

The presence of direct and resolved photon processes suggests a substantial amount of hard scattering in photoproduction. H1 [6,51] and ZEUS [52] analyzed the transverse momentum behavior of events from photoproduction and ep scattering at low Q^2.

8.1 H1 analysis

The study was made with two event samples recorded for a total luminosity of 0.9 nb^{-1}. The selection criteria for sample I were:

- the scattered electron detected in LUMI
- a track from the interaction region
- $0.35 < y_e < 0.7$ and $y_h > 0.2$

  where y is the scaled photon energy $y = \nu/\nu_{max}$

  calculated from the scattered electron $y_e = 1 - E_e'/E_e(1 + \cos\theta e')/2$

  from the hadrons meas'd in calorimeter $y_h = \Sigma\,(E^i - p_L{}^i) / (2\,E_e)$
- energy > 5 GeV in the forward region ($\theta < 25^o$).

A total of 330 events satisfied the requirements.The background from beam gas interactions was estimated to be < 9%. Tagging of the scattered electron in LUMI ensures the events to come from photoproduction. The range for the c.m. energy W is 175 - 250 GeV.

The transverse momentum distribution is shown in fig. 50. For $p_t^2 < 1$ GeV^2 a steeply falling distribution is observed which is well described by a gaussian with an rms of ~ 350 MeV/c. At higher p_T^2 the data show a second component with a long tail of high transverse momenta indicating the presence of hard scattering. A jet search was performed with the calorimeter requiring jets of more than 3 GeV in cones of $\Delta R = (\Delta\eta^2 + \Delta\phi^2)^{1/2} < 1$ where ϕ is the azimuthal angle. For the 19 events with two or more jets the c.m. energy of the two most energetic jets is on average 12.5 GeV.

Since the photon energy is known, $E_\gamma = E_e - E_e'$, the momenta of the two jets are constrained. At the parton level, equating the jets with partons of equal transverse energy E_t and polar angles θ_1 and θ_2 , and neglecting initial state radiation:

$$2\,E_\gamma/E_t = \tan\theta_1/2 + \tan\theta_2/2.$$

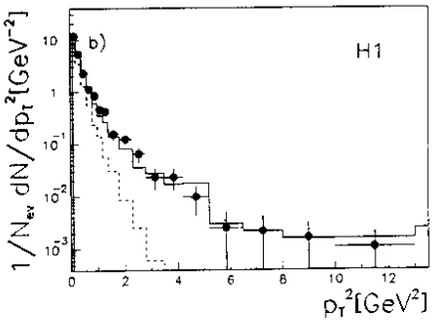

Fig. 50 Squared transverse momentum distribution of charged tracks as observed by H1 from ep data compared with 'soft' (dashed line) and 'soft + QCD' Monte Carlo simulation (full line)

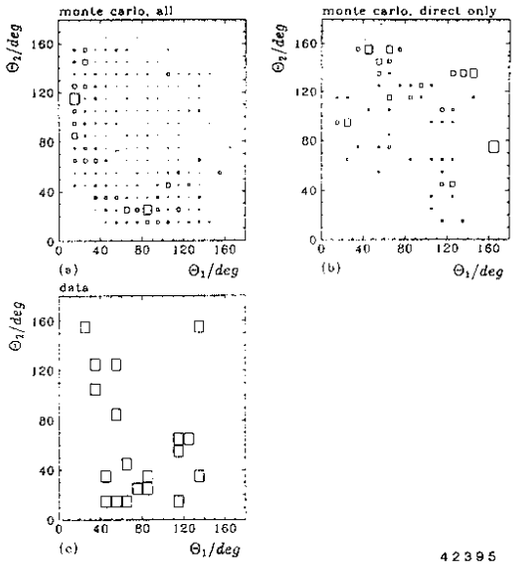

Fig. 51 Correlation of the two highest p_T jets in polar angle for H1 events with an electron tag:
(a) Monte Carlo predictions for resolved and direct processes,
(b) for direct processes only, (c) correlation for the 19 events with a tagged electron.

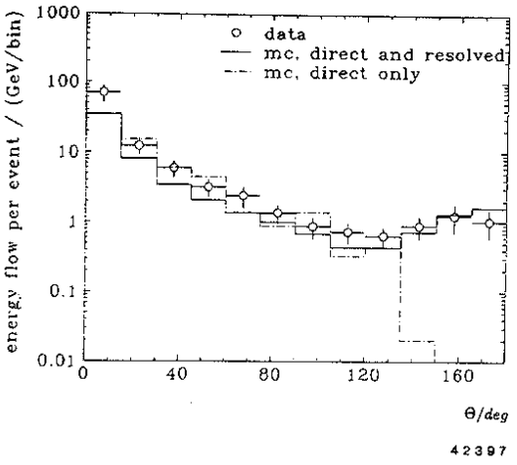

Fig. 52 Energy flow per event versus polar angle as measured by H1; the open points represent the data; the full line is taken from the Monte Carlo simulation for resolved and direct photons; the dotted line gives the prediction for the direct processes alone

Figure 51 shows the distribution of θ_1 versus θ_2 for the data and the predictions for events from direct plus resolved photons and direct photons alone. There is a clear distinction predicted for direct and resolved processes: the direct process yields rarely events where both jet angles are below 100^o : only 0.9 events should be found in this region. Instead, 9 of the 19 measured events lie in this region in agreement with the predictions for the direct and resolved processes.

The indication that the data require a resolved photon contribution has been further substantiated by a second sample (II) for which an electron tagged in LUMI was not demanded; thus, these events are not necessarily from photoproduction. However, events with a substantial Q^2 were removed by requiring that there be no electron with $E > 10$ GeV in $140^o < \theta < 176^o$. A total of 51 event were selected in this way.

Figure 52 shows the energy flow per event as a function of the polar angle θ for events where the two most energetic jet cones have $\theta < 100^o$. In this case the direct process predicts no energy flow beyond $\theta \sim 130^o$ in marked contrast with the data which show a sizeable energy flow up to 180^o. The prediction for the direct *plus* resolved photon processes is in good agreement with the data.

8.2 ZEUS analysis

The events were selected by requiring in addition to the calorimeter trigger

- proper timing observed by the calorimeter,
- more than 10 GeV in FCAL and > 2.5 GeV in RCAL,
  or: > 20 GeV in total energy, > 10 GeV in total transverse energy and $\Sigma (E^i - p_L^i) / (2 E_e) > 12$ GeV when summed over all calorimeter cells,
- no scattered electron observed in the calorimeter with $y_e < 0.7$. This cut ensures that the accepted events have $Q^2 < 4$ GeV^2.

The cuts were satisfied by 576 events from a total luminosity of 2.2 nb^{-1}. The contamination from beam gas events is < 3% and < 2% from deep inelastic events with $Q^2 > 4$ GeV^2.

The data are consistent with originating from photoproduction. This is shown by comparing the full sample with the 96 events for which the scattered electron was detected in LUMI with $5 < E_e' < 22$ GeV. These events have $Q^2 < 0.02$ GeV^2. The ratio of tagged to total number of events agrees well with the Monte Carlo prediction of 20% for pure photoproduction events. The distribution of the γp c.m. energy W is shown in fig. 53a. For the full sample W is in the range from 100 to 295 GeV; for the tagged electron events it is narrower, $160 < W < 260$ GeV, reflecting the restricted electron energy range. Deep inelastic events would have a completely different shape, peaking sharply at small W.

The distributions of the total transverse energy E_T and the missing transverse momentum p_{Tmis} are shown in figs. 53b,c. The overall p_T is well balanced as expected for photoproduction, the average p_{Tmis} being 1.5 GeV/c. The

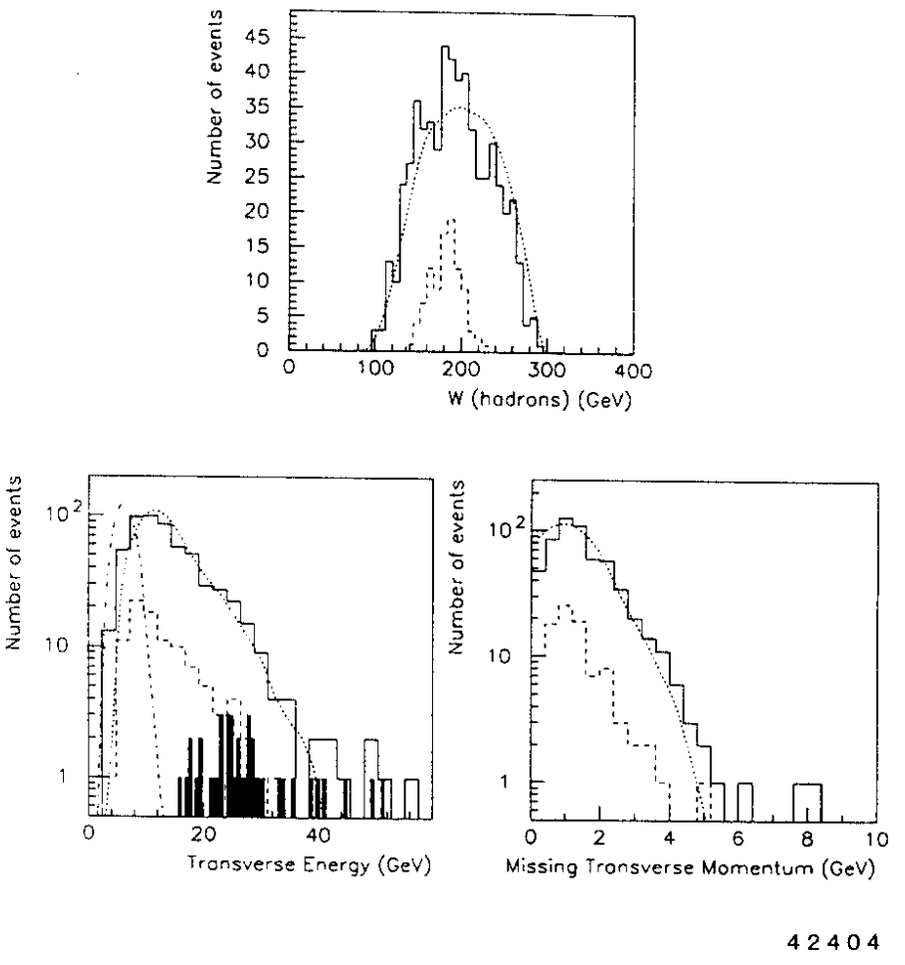

Fig. 53 Hard scattering in photoproduction as analyzed by ZEUS:
(a) Distribution of the γp c.m. energy W for all events (solid histogram) and for events with a tagged electron (dashed histrogram) ; the curves show the Monte Carlo expectations;
(b) Total transverse energy distribution for all events (solid histogram) and for events with a tagged electron (dashed histogram), and for events with a twojet structure (black histogram); the dashed curve shows the expectations from the Monte Carlo simulation including direct and resolved photon contributions with p_{Tmin} = 1.5 GeV/c ; the dashed-dotted curve shows the transverse energy distribution for soft γp interactions

E_T distribution exhibits, by contrast, a tail that extends beyond 10 GeV: 391 events have $E_T > 10$ GeV. The tagged electron events show the same behavior (dashed histogram). The tail is much larger than that expected from soft γp interactions which extends to a maximum of 10 GeV (dashed-dotted curve in fig. 53b). A comparison of the cross sections shows that 20 % of all photoproduction events have an $E_T > 10$ GeV.

The events were searched for jets with jet cone $\Delta R < 1$, jet transverse momentum > 4 GeV and $\eta < 2$ ($\theta > 15^0$): 41 events were found with two jets. One of these events is shown in fig. 54a displaying two clear jets. The distributions of the jet transverse momenta and azimuthal angles are shown in fig. 55b,c for the two - jet sample. The jets are predominantly back-to-back in the transverse plane. The E_T values for the two - jet events are all above 16 GeV as shown by the black histogram in fig. 53b.

As discussed before, a major fraction of the high E_T events is expected to come from resolved photon interactions and therefore to show substantial energy flow in the backward (electron beam) direction from the photon remnants. Figure 55d shows the energy deposited in the RCAL (rear calorimeter) versus the minimum pseudorapidity η of either of the two jets. Note, jets in the forward hemisphere have $\eta > 0$, and in the backward hemisphere $\eta < 0$. If direct photon interactions were the sole origin of these events, sizeable energy in RCAL would be expected for events with the minimum $\eta_{min} < -1$, falling essentially to zero as the jets become more distant from the RCAL region ($\eta_{min} > 0$). This trend is indeed observed in fig. 55d. However, in addition the data show events with as much as 4 - 12 GeV detected in RCAL, even when both jets are far from the RCAL itself, the nearest jet being as much as three units of rapidity away. These events are interpreted as originating from the resolved photon process, where the two partons go forward and the photon remnants go approximately in the direction of the incident electron, which is close to the direction of the photon. One of the resolved photon candidates is shown in fig. 54b. It has two jets in the forward direction and a cluster of energy going backward.

8.3 Discussion of the Results

The findings of both experiments are consistent. Photoproduction at c.m. energies of 100 - 300 GeV exhibits an excess of events with large transverse momenta. For a fraction of these events large transverse momentum jets have been observed which is evidence for the presence of hard scattering. In events with two jets the jets tend to be back-to-back in the transverse plane. Although the statistics is limited, there is a clear indication that in some of the events where both jets go forward, in addition a substantial amount of energy is emitted in the backward direction, close to the direction of the incident photon. This event topology is expected for resolved photon processes where the photon remnant goes into the direction of the incident photon.

Hard scattering in photoproduction was predicted to arise from the direct and resolved photon processes. H1 and ZEUS find that the observed gross features

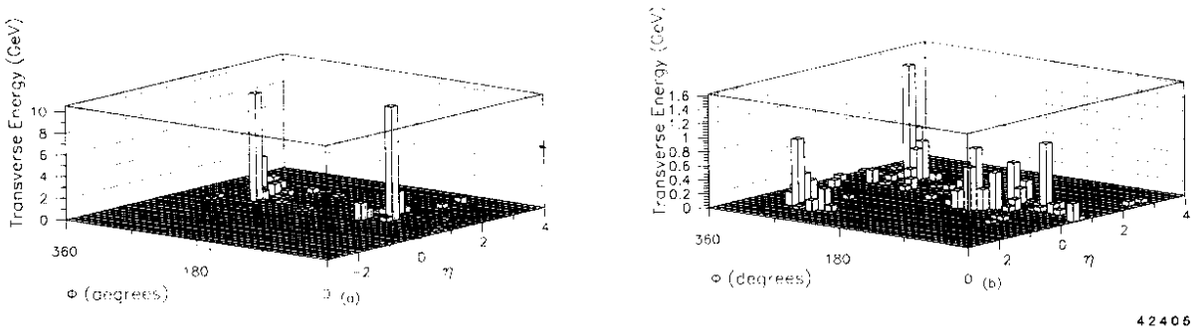

Fig. 54 Examples for events from hard scattering in photoproduction as observed by ZEUS in η - ϕ space:
(a) An event with a two - jet structure;
(b) An event showing a two - jet structure plus additional energy in the direction of the incident electron associated with the photon remnant

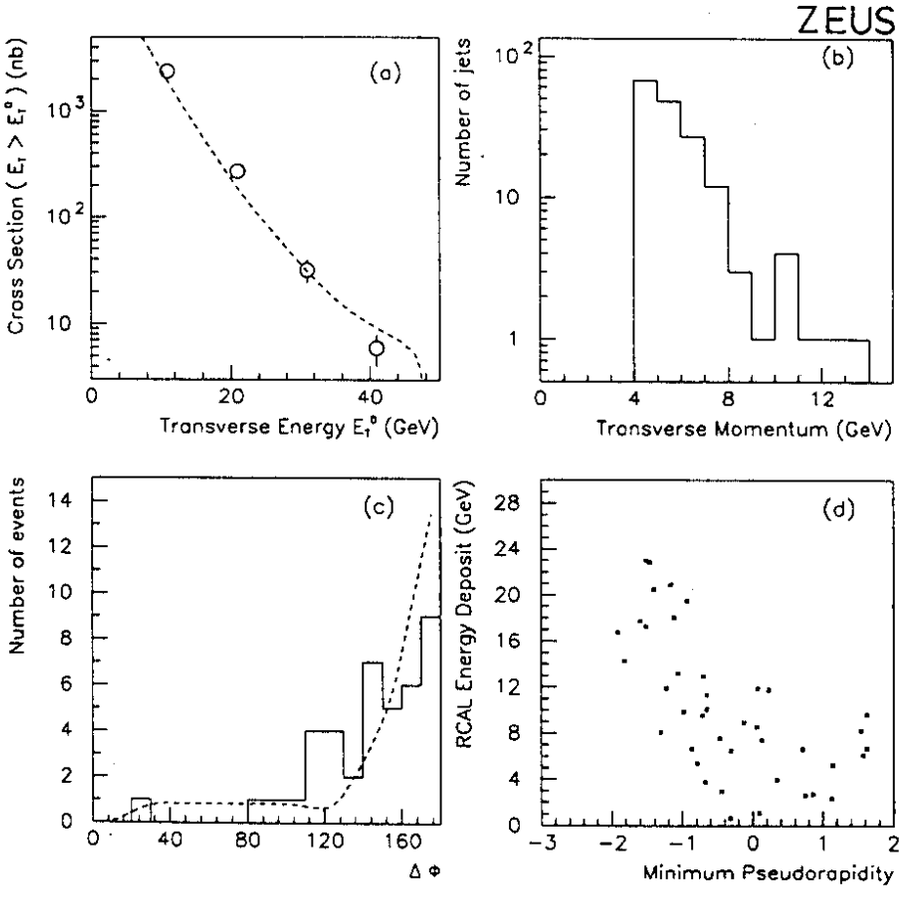

Fig. 55 Hard scattering in photoproduction as analyzed by ZEUS:
(a) Total ep cross section for transverse energies $E_T > E_t^0$. The curve is the cross section predicted by HERWIG with p_{Tmin} = 1.5 GeV/c, including direct and resolved photon contributions.
(b) Transverse momentum distribution of the identified jets;
(c) Distribution of the difference in azimuth between jets for events with two jets; the dotted curve shows the Monte Carlo prediction;
(d) Correlation between energy deposited in the RCAL versus the minimum rapidity of the two jets in the two-jet sample

as well as the cross sections can be accounted for by these processes. They were calculated together with the soft contributions by Monte Carlo in full detail, using the PYTHIA generator[53] (H1) as well as PYTHIA and HERWIG[54] (ZEUS) with the photon structure functions of ref. 48, the proton structure function MTB1 of ref. 30, including initial and final state parton showers, fragmentation into hadrons in the Lund scheme[31], and describing the detector performance within the framework of GEANT[55].

The predictions calculated for a $p_{T\min}$ cutoff of 1.5 GeV/c give a good account of the observed data. This is shown by H1 by the solid curves for the p_T^2 distribution (fig. 50) and the energy flow in two - jet events (fig. 52). The corresponding comparison by ZEUS is shown for the E_T and missing transverse momentum distributions (dashed curve in figs. 53 b,c). H1 has made an absolute comparison with the p_T distribution of jets (fig. 56) and observes agreement within a factor 2 for $p_T > 10$ GeV. ZEUS finds that the cross section for high E_T events is well reproduced by the calculation: fig. 55a compares the data with the prediction for the total ep cross section for E_T values larger than a given E_T^0 energy. If only the direct photon contribution is included the predicted cross section falls short of the measured one by at least an order of magnitude.

In conclusion H1 and ZEUS observed hard scattering in high energy photoproduction at the level of 20% of the total photoproduction cross section. The data are in good qualitative and quantitative agreement with theory which predicted the existence of hard scattering as a result of direct and resolved photon processes. The observed event topologies give an independent indication for the presence of resolved photon contributions.

9. CONCLUDING REMARKS

HERA has joined the family of active high energy colliders and the experiments H1 and ZEUS sofar have encountered no problem to enter a new territory of electron proton collisions. The data which led to the results discussed above were obtained in the first month of data taking. Although the luminosity collected was only a tiny fraction of its nominal value, the experiments presented already exciting results. During the second run period the luminosity rose by a factor of ten and there is good reason for expecting it to rise by several orders of magnitude more in future running. With increasing luminosity more processes will come into the reach of H1 and ZEUS. Examples are deep inelastic neutral scattering where in the beginning every factor of ten increase in luminosity will enlarge the accessible Q2 range by another order of magnitude, and charged current scattering, for which a first candidate with $Q^2 \approx 12\,000$ GeV^2 was observed in the second run period (fig. 57).

Acknowledgements

I am grateful to F. Barreiro, H. Kowalski, E. Lohrmann and F. Sciulli for a critical reading of the manuscript, and to G. Schuler for many comments on the current theoretical picture of photoproduction. S. Gharavi has been helpful with the preparation of the drawings.

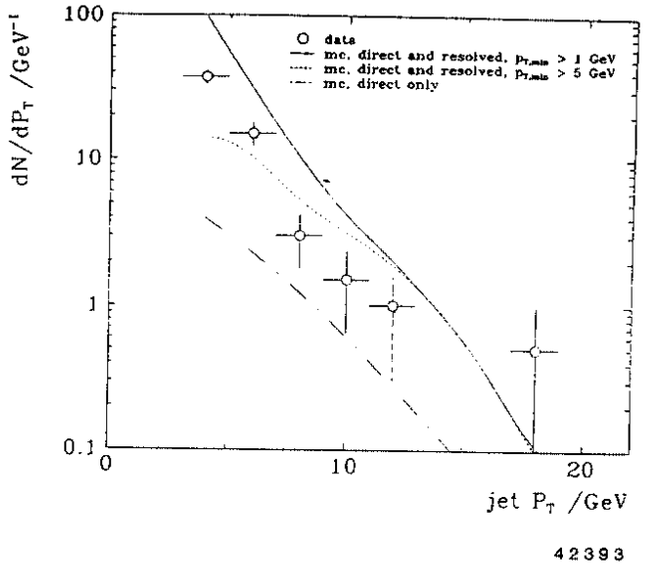

Fig. 56 Hard scattering in photoproduction as analyzed by H1: p_T distribution of jets with $p_T > 3$ GeV. The solid line is the prediction of PYTHIA for $p_{Tmin} = 1$ GeV/c, the dashed dotted line corresponds to $p_{Tmin} = 5$ GeV/c. The dashed - dotted line is the prediction if resolved photon contributions are excluded ($p_{Tmin} = 1$ GeV/c)

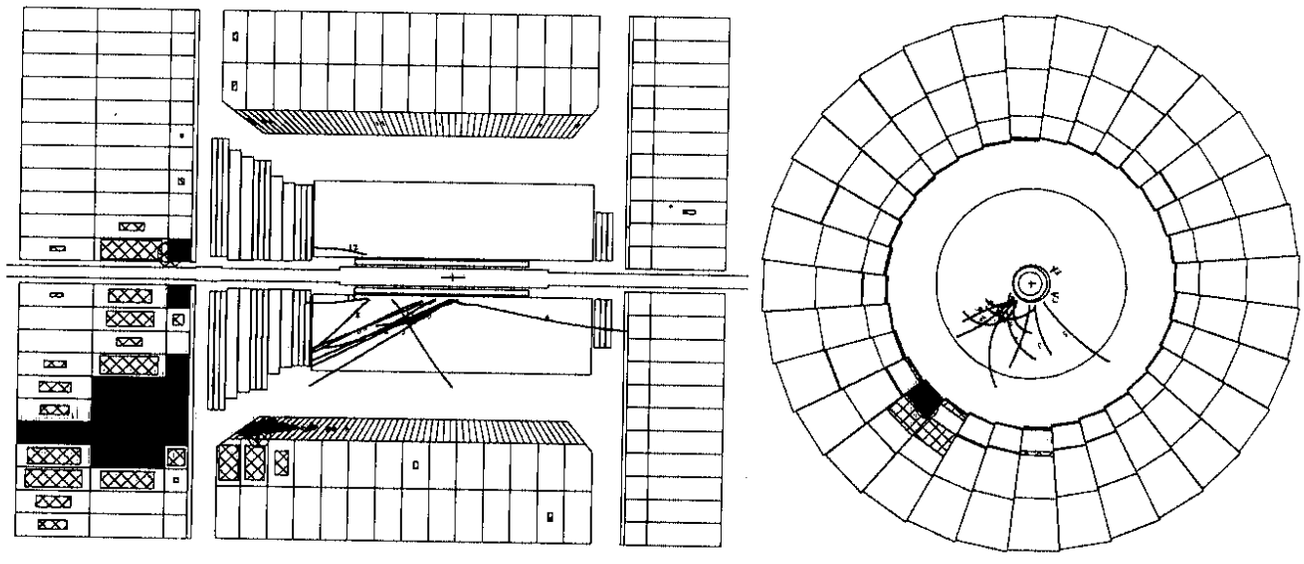

Fig. 57 A charged current event with $Q^2 \approx 12\,000$ GeV^2 observed by ZEUS

REFERENCES

In the following "HERA Workshop 1991" stands for Physics at HERA, Proc . Workshop 1991, ed. by W. Buchmüller and G. Ingelman, April 1992.

1. HERA, A Proposal for a Large Electron - Proton Colliding Beam Facility at DESY, DESY HERA 81 -10 (1981);
   B.H. Wiik, Electron - Proton Colliding Beams, The Physics Programme and the Machine, Proc. 10^{th} SLAC Summer Institute, ed. A. Mosher, 1982, p. 233, and Proc. XXVI Int. Conf. High Energy Physics, Dallas, 1992;
   G. - A. Voss, Proc. First Euro. Acc. Conf., Rome, 1988, p. 7.
2. H1 Collaboration, Technical Proposal for the H1 Detector (1986).
3. ZEUS Collaboration, The ZEUS Detector, Technical Proposal (1986), and: The ZEUS Detector, Status Report 1989.
4. Proc. HERA Workshop 1987, ed. by R. Peccei, August 1988.
5. HERA Workshop 1991
6. H1 collaboration, F. Eisele, Proc. XXVI Int. Conf. High Energy Physics, Dallas, 1992.
7. ZEUS collaboration, B. Löhr, Proc. XXVI Int. Conf. High Energy Physics, Dallas, 1992; I. Gialas, ibid.
8. F. Eisele and G. Wolf, Physikalische Blätter 48 : 787 (1992).
9. HERMES Collaboration, A proposal to measure the spin - dependent structure functions of the neutron and the proton at HERA (1990)
10. A.A. Sokolov and M. Ternov, Sov. Phys. Doklady 8 :1203 (1964).
11. D.B. Barber et al., DESY Report 92 - 136 (1992).
12. J. Buon and K. Steffen, DESY report 85 - 128 (1985).
13. F. Jacquet and A. Blondel, Proc. Study of an ep Facility in Europe, ed. U. Amaldi, 79/48 (1979), p. 391
14. S. Bentvelsen, J. Engelen and P. Kooijman, HERA Workshop 1991, Vol. 1, p.23
15. H. Chaves, R.J. Seifert and G. Zech, HERA Workshop 1991, Vol. 1, p. 57.
16. C.G. Callan and D.G. Gross, Phys. Rev. Lett. 22 : 156 (1969).
17. V.N. Gribov and L.N. Lipatov, Sov. J. Nucl. Phys. 15 : 438, 675 (1972);
    G. Altarelli and G. Parisi, Nucl. Phys. 126 : 297 (1977).
18. J. Blumlein et al., Akad. Wissenschaften, Berlin-Zeuthen, Report 88 - 01 (1988)
19. L.V. Gribov, E.M. Levin, M.G. Ryskin, Phys. Rep. 100 : 1(1983).
20. see e.g.J. Bartels and J. Feltesse, HERA Workshop 1991, Vol 1,p. 131, and references given there.
21. V.T. Kim and M.G. Ryskin, DESY Report 91 - 064 (1991).
22. A.H. Mueller, Proc. Small x - Workshop at DESY, 1990, ed. by A. Ali and J. Bartels, Nucl. Phys. 18C : 125 (1991).
23. NMC Collaboration, P. Amaudruz et al., CERN-PPE/92-124 (1992), submitted to Phys. Lett.
24. J. Kwiecinski et al., Phys. Rev. D42 : 3645 (1992);
    J.G. Morfin and W.K. Tung, Z. Phys. C52 : 13 (1992);
    M. Glück, E. Reya, and A. Vogt, Z. Phys.C48 : 471 (1990).
25. A.D. Martin, R.G. Roberts and W.J. Stirling, Durham University preprint DTP - 92 -16 (1992).
26. L.N. Lipatov, Sov. J. Nucl. Phys. 23 : 338 (1976); E.A. Kuraev, L.N. Lipatov and V.S. Fadin, Sov. Phys. JETP 45 : 199 (1977); Y.Y.
    Balitskii and L.N. Lipatov, Sov. J. Nucl. Phys. 28 : 822 (1978).
27. ZEUS Collaboration, M. Derrick et al., DESY Report 92 - 180 (1992).
28. H1 Collaboration, T. Ahmed et al., DESY Report 92 - 164 (1992).
29. H1 Collaboration, T. Ahmed et al., DESY Report 92 - 162 (1992).
30. J.G. Morfin and W.K. Tung, Z. Phys. C52 : 13 (1992).

31. T. Sjöstrand, Comp. Phys. Com. 39 : 347 (1986); T. Sjöstrand and M. Bengtsson, ibid 43 : 367 (1987) and CERN-TH 6488/92 (1992).
32. A. Kwiatkowski, H. Spiesberger and H.-J. Möhring, Comp. Phys. Com. 69 : 155 (1992), and references given there.
33. G. Ingelman, LEPTO5.2, program manual, unpublished; H. Bengtsson, G. Ingelman and T. Sjöstrand, Nucl. Phys. B301 : 554 (1988).
34. L. Lönnblad, Comp. Phys. Com. 71 : 15 (1992), and references given there.
35. G. Ingelman, HERA Workshop 1991, Vol. 3, p.1366, and references given there.
36. see F. Schrempp, HERA Workshop 1991, Vol. 2, p. 1034, and references given there.
37. ZEUS Collaboration, I. Gialas, Proc. XXVI Int. Conf. High Energy Physics, Dallas, 1992.
38. G. Schuler, HERA Workshop 1991, Vol. 1, p. 131.
39. Chacaltaya and Pamir collaborations, contribution to VI Int. Symp. on V. H. E. Cosmic Ray Interactions, ICRR-Rpt-216-90-9, 1990.
40. G. Yodh, Nucl. Phys. B (Proc. Suppl.) 12 : 277 (1990).
41. M. Drees, F. Halzen, and K. Hikasa, Phys. Rev. D39 : 1310 (1989);
T.K. Gaisser et al., Phys. Lett. 243 : 444 (1990);
R. Ghandi et al., Phys. Rev. D42 : 263 (1990).
42. ZEUS Collaboration, M. Derrick et al., Phys. Lett. B293 : 465 (1992).
43. H1 Collaboration, T. Ahmed et al., DESY Report 92 - 160 (1992).
44. S. I. Alekhin et al., CERN - HERA 87 - 01 (1987) and references given there.
45. A. Donnachie and P.V. Landshoff, Nucl. Phys. B244 : 322 (1984).
46. H. Abramowicz et al., Phys. Lett. B269 : 465 (1991).
47. M. Drees and K. Grassie, Z. Phys. C28 : 451 (1985);
R.S. Fletcher etal., Phys. Rev. D45 : 377 (1992);
R. Ghandi and I. Sarcevic, Phys. Rev. D44 : R10 :
J.R. Forshaw and J.K. Storrow, Phys. Lett. B268 : 116 (1991);
G. Schuler and J. Terron, HERA Workshop 1991, Vol. 1, p. 599.
48. M. Drees and K. Grassie, Z. Phys. C28 : 451 (1985).
49. H. Abramowicz, K. Charchula and A. Levy, Phys. Lett. B269 : 458 (1991).
50. G. Schuler and J. Terron, HERA Workshop 1991, Vol. 1, p. 599.
51. H1 Collaboration, T. Ahmed et al., DESY Report 92 - 142 (1992).
52. ZEUS Collaboration, M. Derrick et al., DESY Report 92 - 138 (1992), submitted to Phys. Lett.
53. T. Sjöstrand, HERA Workshop 1991, Vol. 3, p. 1405.
54. G. Marchesini et al. Comp. Phys. Comm., 67 : 465 (1992).
55. GEANT program manual, CERN program library (1992).\